Silicon and hybrid silicon photonic devices for intra-datacenter applications: state of the art and perspectives [Invited]

Yu Li,[1] Yu Zhang,[1] Lei Zhang,[1,2] and Andrew W. Poon[1,*]

[1]*Photonic Device Laboratory, Department of Electronic and Computer Engineering, The Hong Kong University of Science and Technology, Hong Kong, China*
[2]*State Key Laboratory on Integrated Optoelectronics, Institute of Semiconductors, Chinese Academy of Sciences, P.O. Box 912, Beijing, China*
**Corresponding author: eeawpoon@ust.hk*

Received April 3, 2015; revised May 29, 2015; accepted June 5, 2015; posted June 26, 2015 (Doc. ID 237213); published July 31, 2015

We review the state of the art and our perspectives on silicon and hybrid silicon photonic devices for optical interconnects in datacenters. After a brief discussion of the key requirements for intra-datacenter optical interconnects, we propose a wavelength-division-multiplexing (WDM)-based optical interconnect for intra-datacenter applications. Following our proposed interconnects configuration, the bulk of the review emphasizes recent developments concerning on-chip hybrid silicon microlasers and WDM transmitters, and silicon photonic switch fabrics for intra-datacenters. For hybrid silicon microlasers and WDM transmitters, we outline the remaining challenges and key issues toward realizing low power consumption, direct modulation, and integration of multi-wavelength microlaser arrays. For silicon photonic switch fabrics, we review various topologies and configurations of high-port-count N-by-N switch fabrics using Mach–Zehnder interferometers and microring resonators as switch elements, and discuss their prospects toward practical implementations with active reconfiguration. For the microring-based switch fabrics, we review recent developments of active stabilization schemes at the subsystem level. Last, we outline several large challenges and problems for silicon and hybrid silicon photonics to meet for intra-datacenter applications and propose potential solutions. © 2015 Chinese Laser Press

OCIS codes: (200.4650) Optical interconnects; (230.3120) Integrated optics devices; (130.0250) Optoelectronics; (140.2010) Diode laser arrays; (140.2020) Diode lasers; (140.3410) Laser resonators.
http://dx.doi.org/10.1364/PRJ.3.000B10

1. INTRODUCTION

Currently, warehouse-level datacenters, such as those owned by Google, Facebook, and Amazon, are powered by millions of servers, interconnected over distances of a few kilometers to 10 km. Intra-datacenter interconnects play a key role in determining the performance and scalability of these datacenters. As the number of hosted applications and the amount of traffic in datacenters continuously grow, the industry is now looking for an interconnect solution that supports an ever-larger number of servers at an ever-higher bit rate.

Compared with electrical interconnects, optical interconnects offer the key merits of a high data rate, low latency, and a compact size. They have been viewed as a promising way to overcome the bottleneck of traditional electrical links in short-reach data-intensive applications in datacenters [1,2].

Over the past few years, intensive research and development (R & D) efforts on optical interconnects have resulted in active optical cables for high-speed, energy-efficient, short-reach (a few meters to a few hundred meters) datacenter applications. Both Finisar [3] and Fujitsu [4] have commercialized 4×25 Gb/s transceiver links based on vertical-cavity surface-emitting lasers (VCSELs). However, VCSEL-based optical interconnects transmitting in multimode optical fibers are typically limited to a link distance of below 300 m for a data rate of about 20 Gb/s, rendering them unsuitable for intra-datacenter applications that require a link distance of up to ~10 km.

Instead of VCSEL-based optical interconnects, companies including Molex, Luxtera, Cisco, and Intel have commercialized active optical cables based on silicon photonics for short-reach data-intensive applications. Molex and Luxtera have announced 4×25 Gb/s transceivers with a link distance of up to 4 km upon a total power consumption of ~1 W. Cisco offers a coarse wavelength-division-multiplexing (WDM)-based transceiver with up to 10 km connection upon ~3 W of power consumption. The collaboration among Intel, UCSB, and Aurrion has first demonstrated a transceiver module with a data rate of up to 50 Gb/s [5], and later improved to a data rate of 100 Gb/s [6]. These emergent silicon photonics products leverage the mature complementary metal-oxide-semiconductor (CMOS) nanofabrication technology with well-developed design tools and process recipes. They can be mass manufactured at a low cost using foundry services.

As a photonic material, silicon with an indirect bandgap of ~1.1 eV is essentially transparent in the conventional telecommunications wavelengths (1.3/1.55 μm), rendering low material absorption loss. The high refractive index contrast between silicon (3.45) and its native oxide, silica (1.44), enables a tight optical confinement in small waveguides and photonic structures fabricated on silicon chips, most commonly on silicon-on-insulator (SOI) chips. Over the past 15 years

 © 2015 Chinese Laser Press

or so, founded on the early pioneering work by Soref and colleagues dating back to the 1980s [7–9], a myriad of silicon photonic devices have been demonstrated, including WDM filters [10,11], high-speed electro-optical (EO) modulators [12,13], and reconfigurable EO/thermo-optical (TO) switches and routers [14–22].

It is feasible to enhance the functionalities of silicon photonics by integrating silicon with other materials, including silicon nitride (SiN), silicon oxynitride (SiON), III–V compound semiconductors, and other group-IV elements such as germanium (Ge), tin (Sn), and carbon (e.g., diamond, graphene, carbon nanotubes). For example, epitaxially grown Ge on silicon has been widely used for high-speed photodetection on silicon photonic chips. The bias voltage of Ge-on-silicon photodetectors can be as low as zero [23], making them favorable for integration with CMOS drivers. The Ge-on-silicon platform also offers high-speed EO modulators using the Franz–Keldysh effect [24]. Graphene-based high-speed EO modulators and photodetectors have also been demonstrated [25]. Although Ge-on-silicon and GeSn-on-silicon platforms have been demonstrated for light emission at 1550 nm [26] or longer wavelengths [27], their performance so far cannot compete with those built on the InGaAs/InP platform. By hybrid integrating of silicon with InGaAs-based gain materials, researchers have now demonstrated a host of on-chip hybrid silicon microlasers that emit in a single mode upon relatively low power consumption.

In this paper, we seek to give a bird's eye view on the state of the art of silicon and hybrid silicon photonic devices for optical interconnects in datacenters. Given the rapid development of the field, the scope of our review is by no means exhaustive. Our current research interests mostly drive the choice of topics in this review, with emphasis on recent developments in hybrid silicon microlasers and silicon switches and routers. In this review, we focus mainly on the work applying WDM techniques with the simplest modulation format in on–off keying (OOK). Although there are other emerging multiplexing techniques, such as mode-division multiplexing (MDM) and polarization-division multiplexing (PDM), we do not include these techniques given the limited scope of this review. We also do not include recent work on advanced modulation formats, which need more sophisticated device and subsystem designs for sources, modulators, and detectors. We do not include optical receivers and modulators in the review as there are recent reviews [28–30] covering such topics.

In Section 2, we give a brief summary of the key requirements of optical interconnects for datacenters. Based on the key requirements, in Section 3 we put forth our vision toward a WDM-based optical interconnect for intra-datacenters with a high port count and a high data rate. In Section 4, we review the recent progress, key requirements, and challenges of hybrid silicon lasers for WDM-based transmitters. We discuss key issues regarding material platforms, power consumption, direct modulation, and multichannel transmitters. In Section 5, we review the recent developments in high-port-count silicon photonic switch fabrics, including various topologies and configurations using Mach–Zehnder interferometers (MZIs) and microring resonators as switch elements. We discuss the issue of reliability of high-port-count switch fabrics using microring resonators and review active resonance wavelength stabilization schemes for microrings. In Section 6, we propose what breakthroughs, capabilities, and technical developments are still needed in silicon and hybrid silicon photonics to address the challenges encountered. We conclude the paper in Section 7.

Table 1. Key Requirements for Intra-Datacenter Optical Links

Aggregate Data Rate per Server (Gb/s)	≥100
Power Consumption (fJ/bit)	~625
Link Distance (km)	~10
Wavelength Range (nm)	1300–1600

2. KEY REQUIREMENTS

Here, we list in Table 1 the key requirements for intra-datacenter optical interconnects concerning (1) aggregate data rate per server, (2) power consumption, (3) link distance, and (4) wavelength range.

Currently, hybrid silicon WDM transmitters applicable to interconnecting servers in datacenters are capable for an aggregate data rate of up to 100 Gb/s, with each of the four wavelength channels modulated at up to 25 Gb/s [6]. Intel Inc. [31] predicted that the number of wavelength channels and the single-channel data rate would reach 16 and 25 Gb/s, respectively, for emergent 400 Gb/s applications, and would increase to 25 and 40 Gb/s, respectively, for 1 Tb/s applications.

In terms of power consumption for intra-datacenter interconnects, Cisco Inc. [32] predicted that by 2020 the total power consumption would reach 2 MW with a bandwidth of 400 Pbytes/s, corresponding to a power consumption of ~625 fJ/bit.

The link distance required is up to ~10 km in order to interconnect servers that are far apart in a warehouse-level datacenter. With the required high data rate and the long link distance, transmission in single-mode fibers is necessary. The laser wavelength range of 1300–1600 nm essentially follows the communications wavelengths in silica optical fibers. However, new transmitter technologies still need to be developed for intra-datacenter applications, as we review below.

3. WDM-BASED OPTICAL INTERCONNECT

Figure 1 illustrates our vision of a WDM-based optical interconnect with a high-port-count routing scheme for intra-datacenter applications. Figure 1(a) shows that each of the N servers is connected with an optical transceiver and is interconnected through an $N \times N$ switch fabric. Here we assume a switch fabric in a cross bar configuration. Following the state of the art, we illustrate each of the transmitters with four directly modulated laser sources emitting at carrier wavelengths that are equally spaced. This requires $4N$ different laser wavelengths in total. The laser wavelength spacing matches the free spectral range (FSR) of the switch elements in the switch fabric, as shown in Fig. 1(b).

Switching the switch elements on or off reconfigures the router optical paths. Figure 1(a) shows as an example a particular configuration of the transmission routes. On the receiver end of each transceiver, the four-channel demultiplexer (DeMUX) with a FSR equal to 4× FSR of the switch elements separates the four wavelength channels from a single transmitter and individually detects the channels.

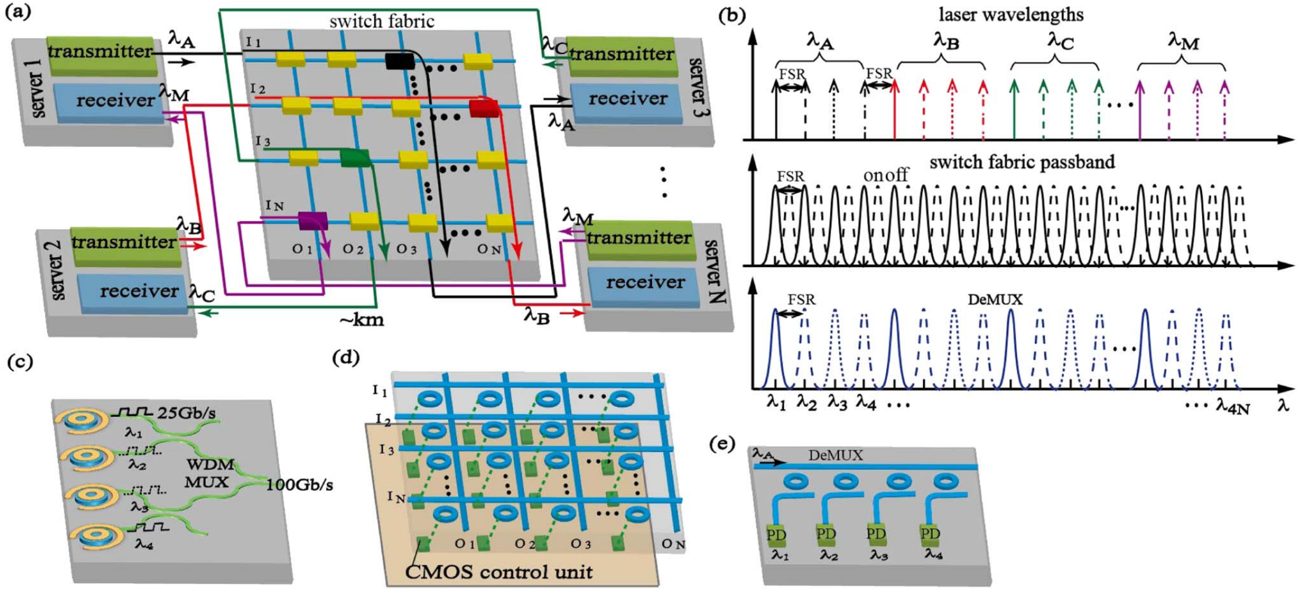

Fig. 1. (a) Schematic of a WDM silicon photonic interconnect for datacenters. N servers connected with optical transceivers are interconnected by an $N \times N$ switch fabric. The black, red, green, and purple lines show different routes from different transmitters emitting in sets of four wavelengths, denoted as λ_A, λ_B, λ_C, and λ_M, respectively. The colored blocks represent the "on" state of a switch element in the route. (b) Schematic spectra of the laser wavelengths output from the transmitters (upper), the switch fabric transmission bands at the "on" (solid) and "off" (dashed) states (middle), and the filter passbands of the DeMUX at the receiver (lower). The solid, dashed, dotted, and dashed–dotted arrows in the upper figure represent different wavelength channels from a single transmitter. The solid, dashed, dotted and dashed–dotted lines in the lower figure represent the filter passbands in a DeMUX. (c)–(e) Schematic view of (c) a four-channel direct-modulated (DM) transmitter at 100 Gb/s, (d) an $N \times N$ switch fabric using silicon microrings in a cross-bar topology with monolithically integrated CMOS control units, and (e) a four-channel receiver with a microring-based DeMUX and four integrated photodetectors (PDs).

Figure 1(c) illustrates as an example a hybrid silicon multi-wavelength (four-channel) transmitter module with direct modulation at a channel rate of 25 Gb/s. The four transmitter channels are integrated with a WDM multiplexer (MUX) in order to output-couple the wavelength channels to a single-mode waveguide at an aggregate data rate of 100 Gb/s. Figure 1(d) illustrates as an example a silicon-microring-based $N \times N$ switch fabric with monolithically integrated CMOS control units for active reconfiguration and stabilization. Figure 1(e) shows as an example a multichannel hybrid silicon receiver module comprising a silicon-microring-based DeMUX connecting to four photodetectors.

Below we review the state of the art in hybrid silicon lasers and transmitters and high-port-count silicon switch fabrics, which constitute the basis of our conceptual design.

4. HYBRID SILICON LASERS AND WDM TRANSMITTERS

A. Key Requirements

Here we focus our discussion on on-chip hybrid silicon lasers that feature the key merit of not requiring additional photonic packaging, as is required by their off-chip counterparts. Table 2 summarizes the key requirements for transmitters for intra-datacenter applications.

The data rate requirements follow our discussion in Section 2. The number of wavelength channels of each WDM transmitter is larger than or equal to 4 in order to reach the aggregate data rate. Each wavelength channel can be direct modulated (DM) or externally modulated by a modulator at a data rate of 25 Gb/s or beyond.

To satisfy the tight power consumption constraint of ~625 fJ/bit, and assuming the transmitter consumes 60% of the energy, the available energy per bit for an individual laser source in the transmitter (assuming each laser source is modulated in the same way), including all the modulation, wavelength stabilization, and cooling, needs to be ~400 fJ/bit.

Considering the current high-speed photodetector sensitivity and the loss budget requirement for an optical link [33], and taking reference from the 100GBASE-LR4 in IEEE Standard 802.3ba [34] and a non-IEEE standard 100 G CWDM4 MSA [35], we set the minimum average launch power (average power upon modulation) per wavelength channel to be −4 dBm.

For a DM laser, the laser output power upon dc bias equals the average launch power. For an externally modulated laser, the laser output power needs to be higher to compensate for the modulator insertion loss and modulation power penalty [36]. This requires laser output power generally exceeding 0 dBm. We will discuss the power consumption and the output power issues in Section 4.C, and the prospect of DM hybrid silicon lasers in Section 4.D.

Table 2. Key Requirements for Transmitters for Intra-Datacenter Applications

Aggregate Data Rate (Gb/s)	≥100
Data Rate per Channel (Gb/s)	≥25
Channel Number	≥4
Power Consumption (fJ/bit)(including modulation)	~400
Average Launch Power per Channel (P_{launch}) (dBm)	> − 4
Output Profile	Single-mode
Link Distance (km)	few–10
Channel Spacing (GHz)	≥200
Wavelength Range (nm)	1300–1600

For a link distance of ~10 km at a high data rate, the laser output profile needs to be single mode for coupling to a single-mode fiber in order to eliminate modal dispersion.

For a single-channel data rate exceeding 25 Gb/s, the WDM channel spacing following the International Telecommunication Union (ITU) grid is typically wider than 200 GHz (1.6 nm in 1550 nm). Following our conceptual scheme as shown in Fig. 1, we can design the laser wavelengths to span ~300 nm in order to fully utilize the communications wavelength range of 1300–1600 nm in silica optical fibers.

Figure 2 shows three possible schemes to build such WDM-based transmitters. The first two schemes use a number of lasers (e.g., four lasers), with each laser output individually modulated and multiplexed into a single output. The lasers can be DM [Fig. 2(a)] or externally modulated by a modulator [Fig. 2(b)]. The second scheme is relatively mature and commonly adopted in currently demonstrated WDM transmitters [5,6]. The third scheme uses a master laser source that coherently generates all the laser lines in a frequency comb, and the output is demultiplexed into N sets of wavelengths (e.g., sets of four wavelengths), with each set sent to a transmitter and each of the wavelengths separately modulated by a wavelength-selective (WS) modulator. We will review and compare the state of the art of these three schemes in Section 4.E.

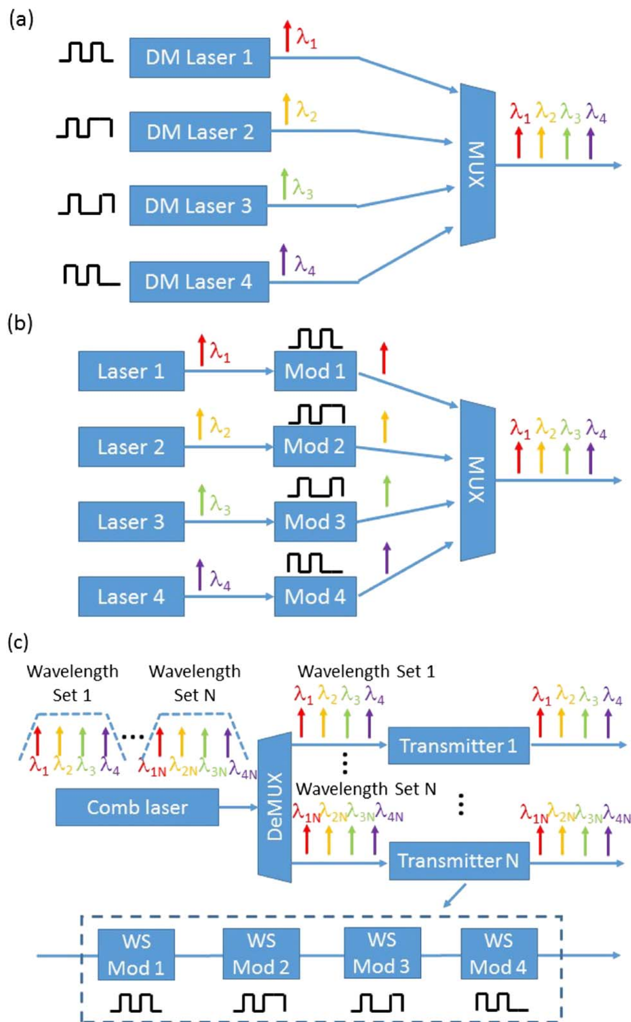

Fig. 2. (a) Schematic of a four-channel WDM-based transmitter with four individual DM lasers and multiplexed into a single output. (b) Schematic of a four-channel WDM-based transmitter with four individual lasers each modulated by an external modulator and multiplexed into a single output. (c) Schematic of N WDM-based transmitters with a master frequency-comb laser demultiplexed into N sets of four-wavelength channels and each set of wavelengths modulated by four WS external modulators.

B. Material Platforms

Here we discuss the material platforms that hybrid silicon lasers are built on. As silicon is an indirect-bandgap semiconductor, it cannot efficiently emit light. Although researchers have explored the possibility of light emission in low-dimensional silicon like silicon nanocrystals [37] or nanopatterned silicon [38], demonstrated devices typically show low light-emission efficiency. One way to enable efficient light emission on silicon substrates is to hybrid integrate with silicon other light-emitting semiconductor materials, such as III–V compound semiconductors or highly strained and heavily doped Ge. Various hybrid silicon on-chip lasers have been realized. The majority of them are based on wafer-bonding technologies [5,39–67] and some are based on epitaxial growth methods [26,68].

1. Wafer-Bonding Technologies

Wafer-bonding technologies by means of (1) molecular bonding [5,39–53], (2) adhesive bonding [54–64], and (3) metallic bonding [65–67] have long been demonstrated for various types of hybrid silicon integrated on-chip light sources with good performance. Figures 3(a)–3(c) illustrate the bonding processes for molecular, adhesive, and metallic bonding.

Molecular bonding uses an oxide layer to bond the III–V and silicon wafers. It requires an extremely smooth bonding

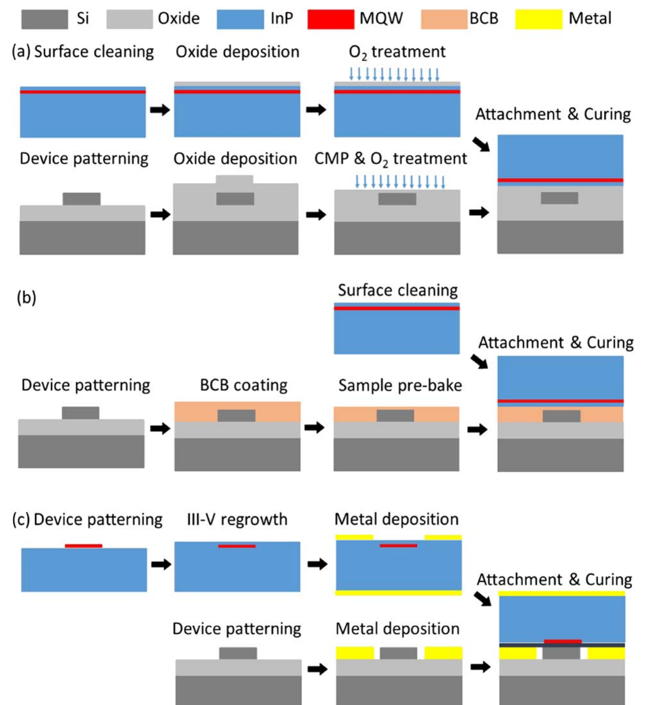

Fig. 3. Schematics of the bonding processes for hybrid silicon lasers realized by (a) molecular bonding, (b) adhesive bonding, and (c) metallic bonding. CMP, chemical-mechanical polishing.

surface, with a typical root-mean-square (RMS) value of less than 1 nm [69]. O_2 plasma treatment is used to activate the bonding surface. It offers high bonding strength with a typical oxide thickness of ~10–100 nm [5,39–53].

Adhesive bonding utilizes thermosetting adhesives to glue the III–V material onto the top of the silicon substrate. Divinylsiloxane-bis-benzocyclobutene (DVS-BCB) is primarily chosen as a superior bonding agent given a high degree of planarization, high bonding strength, and quality (as no by-products are generated during curing). It can tolerate certain surface topography and particles with no special treatment. To our knowledge, the record minimal thickness of the adhesive bonding layer is 40 nm [70]. However, DVS-BCB has a very low thermal conductivity (0.3 W/m/K) [71]. Therefore, the heat dissipation from the BCB-bonded III–V layer is poor. Its glass transition temperature is relatively low at ~350°C [71], making it less stable compared to oxide.

Both molecular and adhesive bonding can be done in wafer-to-wafer, die-to-die, or simultaneous multiple die-to-wafer processes. Therefore, both methods are scalable. They do not need an accurate alignment between the III–V layer and the silicon substrate during the bonding as the III–V devices are fabricated after the bonding.

In contrast, metallic bonding is typically done after individual fabrication of silicon and III–V devices. It needs accurate alignment down to the micrometer level or below. This is not favorable for a multiple die-to-wafer process, which is typically used to overcome the wafer-size mismatch between III–V and silicon wafers. As metal has a high thermal conductivity, the heat dissipation from the metallic-bonded III–V layer is much better than that after molecular and adhesive bonding methods.

To overcome the shortcomings of the conventional metallic bonding of III–V on silicon, researchers from Skorpios Technology Inc. have developed wafer-scale template-assisted bonding [67]. In their processes, pit-receptor sites were first etched on the SOI substrate after silicon layer patterning. Multiple unprocessed III–V dies were mounted on an assembly substrate and then bonded into the pit-receptor sites. Air-gap spacing between the bonded III–V dies and the patterned silicon waveguide were filled by amorphous silicon for low-loss butt coupling. Using this technique, they have demonstrated hybrid silicon lasers with working temperature above 80°C [67].

Table 3 summarizes the typical bonding characteristics of these three bonding methods. Most of the demonstrated hybrid silicon lasers to date are based on molecular or adhesive bonding due to their advantages of a simple process, a low alignment requirement, and scalability.

Table 3. Typical Bonding Characteristics of Molecular, Adhesive, and Metallic Bonding

Bonding Characteristics	Molecular	Adhesive	Metallic
Bonding Strength	High	High	High
Process Complexity	Medium	Low	High
Surface Requirements	High	Low	Low
Alignment Requirements	Low	Low	High
Scalability	High	High	Low
Thermal Dissipation	Medium	Poor	Good
Stability	High	Medium	High

2. III–V-to-Silicon Coupling Schemes

Based on the wafer-bonding technologies, hybrid silicon lasers primarily adopt two light coupling schemes, namely, evanescent coupling and butt coupling.

Most of the hybrid silicon lasers have adopted the evanescent coupling scheme. In this scheme, the laser cavity can be fabricated in either (i) the III–V gain layers and the laser cavity evanescently coupled to a silicon waveguide underneath or (ii) the silicon layer with the light being amplified by the III–V gain layers evanescently coupled on top. For (i), as the cavities are defined in the III–V layers, it does not fully deploy the mature CMOS fabrication, and the coupling strength is sensitive to the vertical and horizontal alignment. For (ii), as the III–V semiconductor material has a refractive index larger than 3.2, the silicon device layer typically needs to be thicker than 400 nm for good optical confinement in the silicon cavity layer. This imposes a device layer thickness mismatch between the hybrid silicon laser and the SOI photonic components, which are typically fabricated with a silicon layer thickness of less than 340 nm for single-mode operation. To overcome the device layer thickness incompatibility, technology platforms including silicon epitaxial growth for the hybrid silicon region [48] or etch down in the silicon device regions [46] have been adopted.

For the butt-coupling scheme, the laser cavity is typically defined in the silicon layer and butt-coupled to an III–V semiconductor optical amplifier (SOA). In this configuration, demonstrated devices showed a high wall-plug efficiency (~10%) with a high output power (~10 mW), and the silicon device layer can remain below 220 nm of thickness with proper design of the spot-size converter [72,73]. However, the overall footprint of the device is large as the size of the SOA is of the order of a few hundreds of micrometers and the threshold current is of the order of a few tens of mA. Therefore, this butt-coupling scheme is not as favorable for compact low-threshold lasers compared to the evanescent-coupling scheme.

3. Heat-Dissipation Issues

One major issue for hybrid silicon lasers built on the molecular or adhesive bonding platform is heat dissipation. Although silicon is a better thermal-conducting material compared to InP substrates of the laser gain medium, the buried oxide underneath the silicon in a SOI substrate and the intermediate bonding materials have low thermal conductivity. This results in a high thermal resistance and degrades the hybrid silicon laser performance due to the temperature rise of the laser. To lower the laser thermal resistance, researchers have designed various integrated thermal shunts [49–51,62] or replaced the substrate [74] or the intermediate bonding layer with a high-thermal-conducting material [63].

For thermal-shunt designs, a common design is to use the pad metal to connect the III–V gain material to the silicon substrate. Liang *et al.* [49] obtained a 35% reduction in temperature rise at 10 mA injection with a 2× output power enhancement compared to the laser without a thermal shunt. Recently, they improved their thermal-shunt design and demonstrated a microring laser that can work up to 105°C [50]. Sysak *et al.* [51] used a polysilicon shunt connecting the silicon substrate to the III–V mesa and demonstrated a 25%

reduction in thermal resistance. Silicon-on-diamond substrates [74] and Al_2O_3 heat-dissipation layers [63] have also been studied for improving heat dissipation. With proper laser structures and thermal-shunt designs and material compositions, hybrid silicon lasers can work up to ~100°C [52]. Such designs then enable uncooled operation for on-chip lasers with no extra power consumption for thermal-electric cooling. As on-chip lasers can heat up the silicon layer, and silicon has a high thermal conductivity, it is crucial to thermally isolate such heat sources from other silicon photonic devices.

4. Epitaxial Growth Methods

Epitaxially grown III–V [68] or Ge-on-silicon substrates [26] offer potentially low-cost, large-volume, wafer-level hybrid silicon light sources. Liu *et al.* [68] reported high-performance III–V quantum-dot (QD) lasers grown on silicon, with a threshold current density of ~0.5 kA/cm^2, a maximum output power of exceeding 100 mW, and a working temperature of up to 119°C. Currently, such epitaxial growth approaches are in their infancy. They need a relatively thick buffer layer for material growth and need further developments for integration on the conventional SOI platform.

To partially address the issue for integration, Bowers *et al.* [75] proposed a hybrid growth and bonding approach. The III–V QDs were first grown on a III–V substrate and transferred onto the top of a silicon substrate through bonding techniques. Another practical issue for III–V-grown-on-silicon lasers is the device lifetime. The dislocations induced by the large lattice mismatch between silicon and III–V materials limits the record operational time of fabricated devices to only ~2100 h [68].

C. Laser Power Consumption and Output Power

To meet the power consumption requirement of less than 400 fJ/bit at 25 Gb/s (<10 mW electrical injection power), along with an exceeding –4 dBm average launch power, the laser wall-plug efficiency needs to exceed 4% in a direct-modulation scheme and 10% for an external-modulation scheme. Therefore, a hybrid silicon laser ideally should have a threshold current of 1 mA or below, with a slope efficiency exceeding 70 mW/A for a direct-modulation scheme and 176 mW/A for an external-modulation scheme, assuming a laser bias voltage of 1.5 V.

There are various types of hybrid silicon lasers that can partially satisfy such requirements. In this section, we present a snapshot of two types of hybrid silicon lasers: (i) distributed feedback (DFB)/distributed Bragg reflector (DBR) lasers, as they typically offer high slope efficiency, and (ii) whispering-gallery-mode (WGM) microdisk/microring lasers, as they generally offer a low threshold.

1. Hybrid Silicon DFB/DBR Lasers

Hybrid silicon DFB/DBR lasers are based on grating reflectors. They feature the key merits of single-mode output, with a typical side-mode-suppression ratio (SMSR) of >50 dB [39]. The output power from this type of laser can exceed 10 mW, with a slope efficiency of ~100 mW/A [39,40,46]. After their first demonstration on the hybrid silicon platform by Fang *et al.* [39], such hybrid silicon DFB/DBR lasers have been attracting a lot of R&D interest. Demonstrated devices typically showed a threshold current of a few tens of mA [39,46,76], which is, however, still high compared to our requirements.

To further reduce the threshold current, Zhang *et al.* [40] have shrunk the laser cavity length down to 200 μm. Demonstrated devices showed a typical threshold current of 8.8 mA, with a maximum output power of ~5 mW at 20°C. A threshold current value down to 1.8 mA has been reported by Matsuo *et al.* [41] using an InGaAsP/InP multiple-quantum-well (MQW) DFB laser bonded on a silicon substrate with a cavity length of 120 μm. The reduction in the threshold was mainly due to the reduced quantum-well (QW) region width and the increased optical confinement factor in the QW (using an InP regrowth process). The bonded DFB laser output a ~0.5 mW (–3 dBm) optical power upon a ~13 mW injection power (8 mA upon 1.61 V). This value comes closest to, but does not yet meet, our requirements.

2. Hybrid Silicon WGM Microdisk Lasers

Hybrid silicon WGM microdisk lasers have been intensively investigated due to their key merits of small footprints, typically low threshold currents, potential for high-speed direct modulation, and ready integration with silicon waveguides. Van Campenhout *et al.* [54] reported a hybrid silicon WGM microdisk laser with a threshold current of as low as 0.5 mA, with a footprint of less than 50 μm^2. Integration of such microdisks into an array form with a microdisk number ranging from 4 [42,55] to 16 [56] have been reported. However, the maximum output power of hybrid silicon microdisk lasers demonstrated to date was typically low (< – 4 dBm). The bidirectional emission and the bistability [43] of the WGM microdisk lasers also hinder their potential applications for optical interconnects, which require unidirectional laser emission and laser operation in the linear regime.

To obtain highly efficient unidirectional lasing emission from WGM microdisk lasers, external-feedback structures, such as the tear-drop reflector [43] and a DBR [58], have been used to obtain unidirectional emission from an evanescent-coupled integrated waveguide. Figure 4(a) shows the schematic of a hybrid silicon WGM microdisk laser coupled with an external-feedback structure.

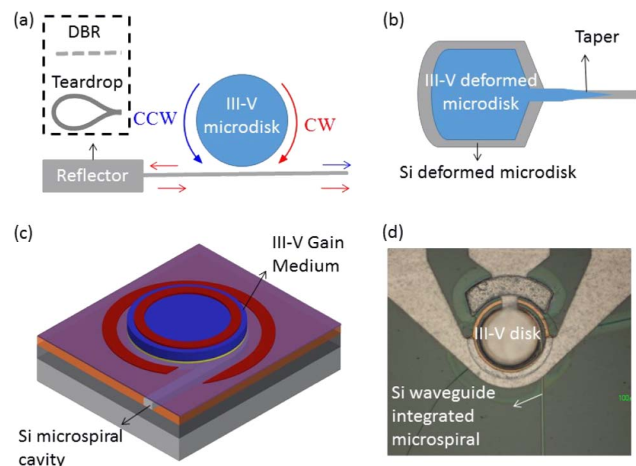

Fig. 4. (a) Schematic of an evanescent waveguide coupled hybrid silicon microdisk laser with a reflector for unidirectional output. CW, clockwise; CCW, counter-clockwise. (b) Schematic of a hybrid silicon deformed microdisk laser. (c) Schematic and (d) optical microscope image of a hybrid silicon microspiral disk laser.

Deformed microdisks offer another promising route toward attaining unidirectional-emission WGM microdisk lasers. Peng *et al.* [59] reported a hybrid silicon unidirectional-emission waveguide-coupled deformed microdisk laser. Figure 4(b) shows the schematic of their deformed microdisk cavities, with a III–V deformed microdisk vertically coupled with a silicon deformed microdisk. Both microdisks were directly coupled with output waveguides that were vertically coupled.

Leveraging the well-studied microspiral disk lasers demonstrated on the III–V platform [77,78], our research group designed and fabricated hybrid silicon-waveguide-coupled microspiral disk lasers [60,61] that can yield unidirectional emission. Figure 4(c) schematically shows the hybrid silicon microspiral disk laser. The silicon microspiral cavity is gaplessly butt-coupled with a silicon waveguide at the microspiral notch. The III–V microdisk gain medium is bonded and evanescently coupled on the top, with a ring-patterned electrode for spatially selective current injection. Figure 4(d) shows the optical micrograph of the fabricated hybrid silicon microspiral disk laser.

A promising way to improve the efficiency of WGM injection microdisk lasers is to preferentially inject current into the WGMs, with a moderate cavity quality (Q) factor and high output efficiency. Theoretical study by Ge *et al.* [79] suggested 185× enhancement in laser output power and some reduction in threshold using spatially selective pumping compared to uniform pumping.

Previously, our research group experimentally demonstrated a $1.5\times$–$2\times$ reduction in threshold and $3\times$–$5\times$ improvement in slope efficiency on III–V microspiral disk lasers using spatially selective injection compared to uniform injection [80]. We are currently experimentally investigating such reduction in threshold and improvement in slope efficiency on hybrid silicon microspiral disk lasers using spatially selective injection [60,61]. To meet the laser output power requirements, we need an at least 3× improvement in slope efficiency from the demonstrated values of the III–V microspiral disk lasers, along with no early power saturation upon up to ∼10 mW electrical injection.

D. DM Hybrid Silicon Lasers

The laser direct-modulation scheme can be more energy efficient than the external-modulation scheme because it saves an at least 4 dB optical loss budget [36] and an external modulator typically requires more than a few tens of fJ/bit extra power consumption [81]. The direct-modulation scheme also offers simpler device configuration with smaller total footprint, making it more favorable for multichannel integration. High-speed DM DFB lasers have been demonstrated on the III–V platform, with a data rate of up to 50 Gb/s [82]. Matsuo *et al.* [83] successfully bonded a high-speed DM DFB laser on silicon substrates, demonstrating up to a 40 Gbps speed with a low power consumption down to 500 fJ/bit (at 25.8 Gb/s).

Direct modulation has also been demonstrated on other types of hybrid silicon lasers. Liu *et al.* [64] demonstrated a DM microdisk laser with a 3 dB bandwidth of 3.5 GHz and clear data transmission waveforms at 1.5 Gb/s. Fang *et al.* [39] have demonstrated a DBR laser directly modulated at 4 Gb/s with a modulation bandwidth of ∼2.5 GHz. Duan *et al.* [46] later improved the modulation bandwidth to ∼7 GHz. Recently, De Valicourt *et al.* [84] reported a 20 Gb/s wavelength-tunable DM hybrid silicon laser. They attributed the enhanced direct-modulation bandwidth to the resonance induced by photon–photon interaction between two spectrally neighbored longitudinal modes of the extended laser cavity. More recently, Zhang *et al.* [40] reported 12.5 Gb/s direct modulation on a short-cavity DFB laser. The extinction ratio (ER) from the DM hybrid silicon lasers demonstrated to date is typically larger than 4 dB, which is considered sufficient for intra-datacenter applications [34,35].

Nevertheless, the direct-modulation speed of hybrid silicon lasers is typically low compared to that of the III–V counterparts. Most of the demonstrated speeds cannot satisfy the channel data rate requirement. A relatively low direct-modulation speed not only impairs the total aggregate data rate from a multichannel transmitter but also has implications on raising the power consumption per bit (as fewer data bits result from a certain dc bias). The low direct-modulation bandwidth is often partly limited by poor heat dissipation. With improved designs for thermal shunts, we expect higher data rates for DM hybrid silicon lasers than demonstrated speeds to date.

Another potential approach to enhancing the direct-modulation bandwidth, especially for WGM microdisk lasers, is to employ spatially selective injection into the lasing mode. Our research group has demonstrated an improved modulation bandwidth from 7.7 to 10.4 GHz on a III–V microspiral disk laser, with a patterned ring electrode selectively injecting to the rim region of the microdisk compared to that with a disk electrode uniformly injecting to the microdisk [80]. Figure 5(a) shows an optical microscope image of a microspiral disk laser after p- and n-contact metal deposition with a ring-shaped electrode design. The spatially selective injected microdisk lasers showed open eye diagrams at 15 Gb/s, as shown in Fig. 5(b). We attribute the bandwidth improvement to the reduced device capacitance given the ring electrodes and the minimized lateral diffusion current between the ring electrodes surrounding the microdisk.

Table 4 summarizes the performance for individual hybrid silicon lasers.

E. Multiwavelength Laser Arrays/Transmitters

Current DM hybrid silicon lasers have relatively low speed. All the WDM hybrid silicon transmitters commercially available to date are externally modulated by either a silicon modulator [5] or a hybrid silicon modulator [6], with a data rate of 12.5 to 25 Gb/s.

Various hybrid silicon WDM laser arrays and transmitters have been demonstrated, most commonly with four laser

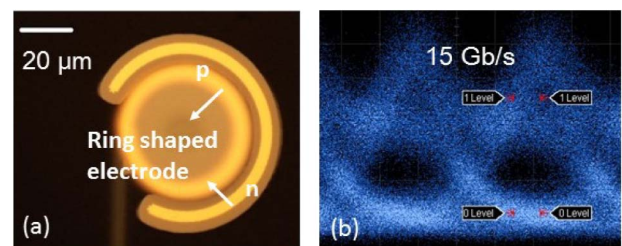

Fig. 5. (a) Optical microscope image of an III–V microspiral disk laser with a ring-shaped p- and n-contact design for spatially selective injection. (b) Measured eye diagram at 15 Gb/s.

Table 4. Summary of State of the Art of Hybrid Silicon Lasers[a]

Mod. Schemes	Institution	Laser Structure	Area (μm^2)	Threshold Current (mA)	Threshold Current Density (kA/cm^2)	Slope Efficiency (mW/A)	Maximum Output Power (mW)	Injection Power for P_{launch} (−4 dBm) (mW)	Direct Mod. Speed (Gb/s)	Energy Consumption per Bit (pJ/bit)
Direct	UCSB, USA [40]	DFB	~800	8.8	1.1	67	5	~22.5	12.5	11 at 12.5 Gb/s
	NTT, Japan [41]	DFB	~96	1.8	1.88	100	1.5	~10	40	0.5 at 25.8 Gb/s 0.75 at 40 Gb/s
	III-V Lab, France [46]	DBR	>680	17	NA	33	5	~40	7[a]	NA
	U Ghent, Belgium [58]	Microdisk	~80	0.5	1.27	5	0.01	NA	1.5	NA
	UIUC, USA [66]	VCSEL	NA	7	NA	300	1.1	~13	5	NA
External	UCSB, USA [39]	DFB	>5040	25	1.4	80	5.5	~62.5	NA	>2.5 at 25 Gb/s
	U Ghent, Belgium [54]	Microdisk	~44	0.5	1.1	25	0.01	NA	NA	NA
	NTT, Japan [53]	Photonic crystal	~0.86	0.031	3.6	2	2.5×10^{-5}	NA	NA	NA

[a]Calculated maximum data rate from the reported measured 3 dB bandwidth.

channels. Some hybrid silicon laser arrays are demonstrated only with continuous-wave outputs. For instance, Kurczveil *et al.* [45] and Keyvaninia *et al.* [57] demonstrated four-wavelength lasers using arrayed waveguide grating (AWG) structures. Keyvaninia *et al.* [57] reported multiwavelength lasers with a four-ring filter array, whereas, some hybrid silicon laser arrays have been demonstrated with data transmission based on the direct- and external-modulation schemes [see Figs. 2(a) and 2(b)].

For the external-modulation scheme, Alduino *et al.* [5] demonstrated the first hybrid silicon transmitter using four DBR lasers, each modulated by a silicon Mach–Zehnder (MZ) modulator at 12.5 Gb/s. The outputs were multiplexed into a waveguide using an echelle grating. Koch *et al.*, [6] later demonstrated an aggregate data rate of up to 100 Gb/s by using hybrid silicon electro-absorption (EA) modulators. Figure 6(a) shows the measured lasing spectrum and eye diagrams at 25 Gb/s of the transmitter reported by Fish *et al.* [6].

For the direct-modulation scheme, Van Campenhout and co-workers [55,64] demonstrated cascaded microdisk laser arrays, with four wavelength channels with a channel spacing of 6 and 8 nm and 1.5 Gb/s data transmission from a DM single microdisk laser. Liang *et al.* [42] reported a four-channel microring-based laser array with a direct modulation bandwidth of up to 4.8 GHz. Recently, Menezo *et al.* [76] demonstrated a four-channel DBR laser array with a 7 GHz direct-modulation bandwidth on a single element.

It is clear that the R&D community is now on the path toward a multiwavelength transmitter with more wavelength channels. For instance, Koch *et al.* [44] demonstrated an eight-channel uncooled laser array with 200 GHz channel spacing. Figure 6(b) shows their measured lasing spectrum from two adjacent eight-channel laser arrays. Using microdisk lasers, Huang *et al.* [56] demonstrated up to 16 wavelength channels. Figure 6(c) shows the optical micrograph of the cascaded 16-microdisk-laser array.

The channel spacing of the demonstrated laser arrays are typically 2–20 nm in order to relax the laser wavelength assignment and the WDM MUX/DeMUX design requirements. However, for dense WDM (DWDM) applications with 200 GHz spacing, accurate alignment between the laser wavelengths and the ITU grid remains crucial and challenging. To accurately control the laser wavelengths, it will be crucial to have an athermal design for the transmitter/laser array and precise fabrication of the laser cavity in silicon [44]. As shown in Fig. 6(b), the lasing wavelength of each individual laser can be locked to the ITU grid with 200 GHz spacing from 20°C to 80°C with such an athermal design.

Another possible way to accurately align the individual laser wavelengths to the ITU grid is to make the laser wavelength tunable. By injecting current into the phase-shifting

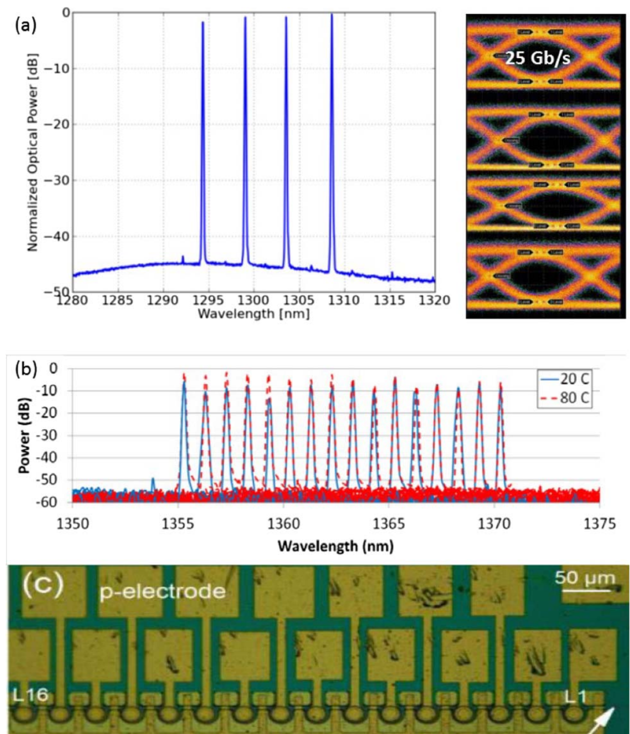

Fig. 6. (a) Measured lasing spectrum and 25 Gb/s eye diagrams of a four-channel WDM transmitter. Reproduced with permission from [6], © IEEE 2014. (b) Measured lasing spectrum of two adjacent eight-channel laser arrays at 20°C and 80°C. Reproduced with permission from [6], © IEEE 2014. (c) Optical micrograph of a 16-channel cascaded microdisk laser array. Reproduced with permission from [56], © IEEE 2015.

section of a DBR laser, Fang *et al.* [39] attained a tuning range of ~13 nm. Keyvaninia *et al.* [47] demonstrated an 8 nm tunable microring laser with a power consumption of ~3 mW/nm. However, we expect the required tuning range for the wavelength alignment purpose is less than 0.8 nm (100 GHz). Therefore, the extra power consumption for tuning can be less than 2.4 mW for the laser demonstrated by Keyvaninia *et al.* [46,47].

Another potential limitation for the transmitter is that the gain bandwidth of a typical InGaAs-based MQW is ~50 nm. To build laser sources emitting from 1300 to 1600 nm with the same epitaxially grown III–V MQW wafer, the gain profile of the wafer needs to be engineered. QW-intermixing techniques have been introduced to spectrally shift the peak of the gain profile. Heavy dopants are implanted or diffused into the QW region to slightly modify the band structure of the QWs and the barriers to modulate the gain profile [85]. Post-implantation annealing is an important factor in precisely controlling the shift of the gain peak and minimize the implantation-induced losses. Chang *et al.* [52] demonstrated wide-range tunable lasing using this technique, with a total wavelength span of up to 200 nm showing adequately uniform laser oscillations.

The performance of each individual laser in a laser array is, however, affected by the uniformity and the yield of the fabrication. Demonstrated laser arrays have typically shown large variations in the output power (>3 dB) and the threshold. Although >95% yield has been obtained for fabricating individual hybrid silicon DFB lasers [86], the same fabrication process can provide a yield of only >80% for a four-channel transmitter. To reliably fabricate laser arrays with high wavelength channel counts, say of 16 or more, the yield of fabricating single lasers needs to be further improved.

Another promising avenue toward realizing compact on-chip multiwavelength sources is to use a frequency-comb laser that generates precisely spaced lasing lines [see Fig. 2(c)] using either mode locking or an on-chip optical parametric oscillator (OPO). Koch *et al.* [87] and Srinivasan *et al.* [88] have demonstrated few-gigahertz to 40 GHz hybrid silicon mode-locked lasers using passive and active mode locking. The outputs of the mode-locked laser can be further stabilized with an external laser injection in order to align with the ITU grid. However, the outputs from the demonstrated mode-locked lasers were highly nonuniform in the spectral domain. The comb lasing line spacing was still too dense (<40 GHz). These render the on-chip mode-locked lasers demonstrated to date less desirable for current WDM intra-datacenter applications. In comparison, an on-chip OPO can generate a wider band of lasing lines with more flexible line spacing. Foster *et al.* [89] demonstrated a 204 GHz spaced frequency comb over 75 THz using a SiN OPO with a 300 mW optical pumped power. Although the line spacing can meet our channel spacing requirements for 25 Gb/s/channel, the lasing output power showed relatively large nonuniformity in the 1300 to 1550 nm range.

Table 5 summarizes the state-of-the-art performance for WDM hybrid silicon laser arrays and transmitters.

5. SILICON OPTICAL SWITCH FABRICS

A. Key Requirements

Silicon optical switches and routers with multiple input ports and multiple output ports have been studied as a critical component for optical data switching among photonic chips, on a photonic chip, and now inside a datacenter [14,17–20,90–94]. Given the increasing data traffic and the huge number of servers in datacenters, high-port-count switch fabrics (e.g., with 32 ports or above) for intra-datacenter optical interconnects are highly desired. However, limited by the stringent application requirements of such switch fabrics, including (i) a high port count number, (ii) a high aggregate data transmission rate at 100 Gb/s/port or beyond, (iii) a fast reconfigurable time of the order of nanoseconds, (iv) low port-to-port insertion loss and crosstalk, (v) a small footprint, (vi) high device uniformity, and (vii) high reliability, until recently, the demonstrated silicon N-by-N switch fabrics are still under relatively low port count of $N = 4$ and 8 ports (see Section 5.D). Table 6 lists the key requirements for high-port-count silicon switch fabrics for intra-datacenter applications.

Here we justify the key requirements listed above. The port count number should well exceed the state of the art, which is currently up to $N = 8$, in order to support the millions of servers and the growing demand for intra-datacenter traffic. Each channel transmission rate should follow the specifications as discussed in Sections 2–4. The channel transmission rate requires the switch element bandwidth to be wider than 0.18 nm in the 1550 nm wavelengths. In addition, the channel transmission rate supports a typical packet duration of less than 20 ns [91], which requires a switch reconfiguration time of the order of nanoseconds.

To support a high port count, the insertion loss and the crosstalk for a port-to-port transmission should be minimized. If we suppose an input optical power of a few milliwatts and a

Table 5. Summary of State of the Art of Hybrid Silicon WDM Transmitters/Laser Arrays

Institution	Laser Cavity Structure	Wavelength (nm)	Footprint (mm^2)	Threshold Current (mA)	Output Power per Channel (mW)	Modulation Scheme	Number of Channels	Data rate per Channel (Gb/s)	Channel Spacing (nm)
Intel, USA [5]	DBR	1310	>1 × 0.6	NA	>2	External	4	12.5	20
Aurrion, USA [44]	NA	1310	NA	<20	>20	External	4	25	4.5
U Ghent, Belgium [55]	Microdisk	1550	0.08 × 0.02	0.9	0.012	Direct	4	1.5	8
III-V Lab, France [76]	DBR	1550	NA	17	4.5	Direct	4	10[a]	12
HP, USA [42]	Microring	1550	0.3 × 0.1	11	0.05–0.3	Direct	4	7[a]	0.8
U Ghent, Belgium [57]	AWG + DBR	1550	0.57	32–42	0.7–3	NA	4	NA	1.6
U Ghent, Belgium [57]	Microring + DBR	1550	1 × 0.2	30–40	2–3	NA	4	NA	2
CAS, China [56]	Microdisk	1550	0.65 × 0.2	11–16	<0.005	NA	16	NA	3

[a]Calculated maximum data rate from the reported measured 3 dB bandwidth.

Table 6. Key Requirements for High-Port-Count Silicon Switch Fabrics for Intra-Datacenter Applications

Port Count Number	≫8
Data Transmission Rate (Gb/s/channel)	≥25
Switch Element Bandwidth (nm)	>0.18
Reconfiguration Time (ns)	~1
Insertion Loss (dB)	< − 20
Crosstalk (dB)	< − 18
Footprint (mm^2)	few tens × few tens

sensitivity of ~ − 16 dBm of a commercial photodetector as the receiver, a port-to-port insertion loss of less than −20 dB would be acceptable [90]. We note that the port-to-port insertion loss is cumulative over all the switch elements along an optical path and is highly dependent on the switch network topology. We analyze in Section 5.C the insertion loss in different network topologies.

For intra-datacenter connections, a bit-error rate (BER) of less than 10^{-8} with a packet loss rate of ~0.01% is desired [95]. Given BER = ½ × exp(-SNR/4) for the OOK system [96], where SNR is the signal-to-noise ratio, and considering that the noise in the port-to-port transmission is contributed mainly by the crosstalk, we require the crosstalk to be smaller than −18 dB.

In addition, the switch fabric footprint is highly related to both the switch network topology and the switch element structure. For instance, the state-of-the-art 8 × 8 switch fabric in switch-and-select network topology using MZIs as switch elements occupies a footprint of 8 mm × 8 mm [16]. Thus, we expect a high-port-count switch fabric should require a footprint of a few tens of millimeters.

Attaining high device uniformity across all the switch elements in a switch fabric is a major requirement. This is still a major hurdle to overcome for silicon photonics fabrication. Although foundry-level silicon photonics fabrication services are becoming accessible worldwide [97,98], the current fabrication processes cannot guarantee a high degree of uniformity over a certain die area. This can introduce significant variations of device performance among the switch elements distributed across a switch fabric, particularly for those occupying a large footprint. Although there are various passive postfabrication trimming techniques to trim silicon photonic devices one at a time [99–101], such approaches are not readily applicable to systematically trim the many switch elements in a switch fabric.

Reliability is also a major criterion in designing a high-port-count switch fabric. The switch performance can be dynamically affected by the real-time chip conditions, such as an on-chip temperature change. To realize reliable operation for high-port-count switch fabrics, it is essential to develop actively stabilized switch elements.

Below we discuss in detail (i) the switch network topologies, (ii) the switch elements, and the state-of-the-art of (iii) high-port-count switch fabrics and (iv) active resonance stabilization schemes for microring-based switch fabrics.

B. Switch Network Topologies

To realize a high-port-count $N \times N$ switch fabric, researchers have explored various topologies over the years. Among these topologies, the four most widely used are (a) Beneš, (b) cross bar, (c) switch-and-select, and (d) dilated Banyan. Figure 7 shows the schematics of the four topologies.

The Beneš topology [15] has been attracting interest recently for use in optical switch fabrics because it is reconfigurable, non-blocking, and requires the minimum number of switch elements in an N-by-N switch system. The Beneš network requires $(2 \log_2 N - 1)$ number of stages, with each stage containing $N/2$ number of 2×2 switches. Figure 7(a) shows a 4×4 switch fabric in Beneš topology, which consists of three stages with six switch elements and two crossings. The Beneš topology features the advantages of the minimum number of switch elements and an equal number of switch elements per light path. This is potentially the most promising topology for high-port-count switch fabrics.

The cross-bar topology, as shown in Fig. 7(b), was among the first topologies explored for high-port-count switch fabrics due to its simple configuration and potential scalability [14,19]. However, the number of switch elements required in a generic cross-bar topology is up to N^2 without network optimization [14]. With $N \gg 1$, the uniformity among the fabricated switch elements would most significantly limit the port count of a cross-bar switch fabric compared with the Beneš topology. Also, the number of switch elements in a transmission path is not a fixed number in a cross-bar network. With a variation from 1 to $2N - 1$ switch elements, the power penalty in different paths varies, resulting in undesirable path-dependent output power levels.

Both the switch-and-select [16] and dilated Banyan [92] topologies, as shown in Figs. 7(c) and 7(d), require $2N(N - 1)$ switch elements in an $N \times N$ switch fabric. One key merit of both topologies is that each switch element sees only a single light path for a certain routing scheme. This eliminates the spatial overlap and interference between two light paths at a switch element, and therefore minimizes the crosstalk. Additionally, both topologies guarantee a fixed switch element number of $2 \log_2 N$ for every transmission path, thus making the insertion loss in principle path independent. However, the required number of switch elements in these two topologies is the largest among the four topologies, making the two topologies less scalable.

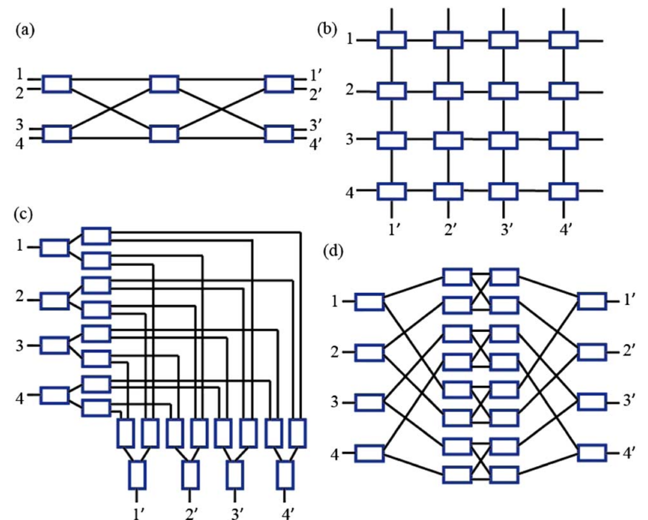

Fig. 7. Schematics of the four common network topologies: (a) Beneš, (b) cross bar, (c) switch-and-select, and (d) dilated Banyan.

Here, we compare the expected performance of the four topologies in terms of the insertion loss and the footprint. We consider as an example a 32-by-32 switch fabric and suppose a total insertion loss budget of 20 dB [90]. Given this, the Beneš topology requires insertion loss of 2.2 dB/switch. The switch-and-select and dilated Banyan topologies require insertion loss of 2 dB/switch. We note that such an insertion loss per switch element is practical as researchers have demonstrated an insertion loss of 0.33 dB/switch [16]. Nonetheless, the cross-bar topology with a longest route that spans 31 switch elements has a relatively stringent insertion loss requirement of less than 0.37 dB/switch.

The footprint of the switch fabric scales up with the required number of switch elements. Here, we roughly estimate the footprint of a 32×32 switch fabric taking into account only the switch element footprint. We use in the analysis a demonstrated MZI-based switch element footprint of 0.02 mm^2 [18]. For the Beneš topology, the footprint would be ~2.9 mm^2 for a total of 144 switch elements. For the switch-and-select and dilated Banyan topologies, the footprint would be ~40 mm^2 for a total of 1984 switch elements, while for the cross bar topology with a switch number of 1024, the footprint would be ~20 mm^2. Therefore, the Beneš topology with a footprint nearly 1 order of magnitude smaller than that of other topologies is advantageous for high-port-count switch fabrics.

We note that all four common network topologies support N-ports-to-N-ports transmission, including self-transmission (i.e., from port-i to port-i). However, for datacenter communications, no self-transmission is needed as data can be processed and switched within the ith server. Therefore, the topologies can be further simplified without the need for self-connection.

C. Switch Elements: Microrings and MZIs

Silicon microring resonators [14,19,20,22] and MZIs [15–18] are the two basic building blocks that are commonly adopted as switch elements in switch fabrics. Figure 8 schematically illustrates basic structures and typical transmission spectra of microring resonators and MZIs. Microring resonators offer the key merits of compact size, relatively low tuning power consumption, and. given their sharp spectral selectivity. can be readily adopted in a WDM system. Currently, the reported silicon microring resonator size ranges from ~1.5 μm [102] to over tens of micrometers. However, the main shortcoming of microring resonators is that the sharp resonances also make them difficult to align with the transmission channels. Also, a single-microring resonance with a sharp Lorentzian lineshape is not favorable in a high-speed data transmission system that prefers flat-top switches in order to minimize the signal waveform distortion and thus the data transmission errors.

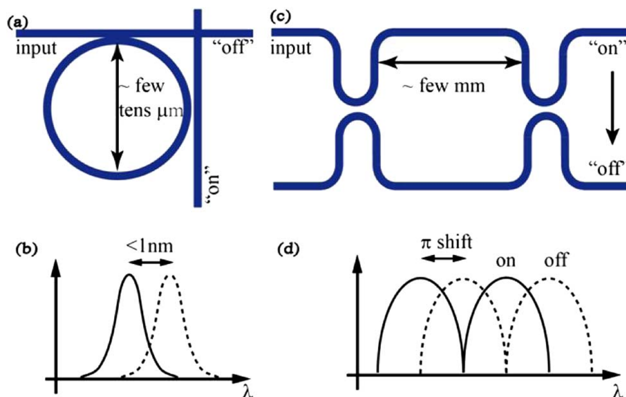

Fig. 8. Schematics of (a) a microring coupled to a waveguide crossing, and (b) "on" (solid) and "off" (dashed) state transmission spectra of a microring switch element. Schematics of (c) a MZI and (d) "on" (solid) and "off" (dashed) state transmission spectra of a MZI switch element.

Whereas MZIs offer the key merit of a relatively wide transmission band compared to that of microring resonators, silicon MZI switch elements typically occupy a footprint in the scale of millimeters, imposed by EO phase-shifter arm length. Switching between the transmission "on" and "off" states thus has a relatively large power consumption. Dong *et al.* [103] showed that EO switching power dropped with an increase in the MZI switch element arm length. They reported a switching power of 0.6 mW for a MZI arm length of 4 mm.

In addition, the MZI arm length is related to crosstalk between the transmission states. Theoretical calculations [104] suggest that with an EO phase-shifter arm length shorter than 1 mm, it is difficult to obtain crosstalk below −30 dB, due to the weak free-carrier-dispersion effect in silicon.

Therefore, compared to a silicon microring resonator with micrometer-size dimensions, the large footprint of a silicon MZI with an millimeters-long arm length renders a MZI switch element less favorable for high-port-count switch fabrics.

D. State of the Art

In the past few years, various research groups have demonstrated high-port-count silicon switch fabrics using MZIs or microrings. Here we review the state of the art. Table 7 summarizes the key methods and performance of the state-of-the-art high-port-count silicon switch fabrics.

1. Switch Fabrics Using MZIs

Lu *et al.* [15] demonstrated a 4×4 switch fabric based on the Beneš topology using MZI switch elements. They used EO phase shifters to realize reconfiguration times on the nanosecond scale with a switch power consumption of 4.5–8.1 mW/switch. However, a TO tuner integrated along each arm of the MZI was used to set the initial phase condition for each MZI. The TO tuner not only increased the MZI footprint but also increased the total power consumption of the switch fabric to 72.2 mW. The footprint of the switch fabric was 3.5 mm × 1.4 mm.

Chen and Chen [16] demonstrated an 8×8 switch fabric based on the switch-and-select topology using MZI switch elements. Leveraging the merit of low crosstalk in a switch-and-select topology, they obtained a port-to-port isolation exceeding 30 dB over an 80 nm transmission band. They demonstrated power consumption per path switching of 1.5 mW. The footprint of the device was 8 mm × 8 mm.

In addition to the four common switch topologies, researchers have demonstrated other switch fabric architectures using MZI switch elements tailored for a specific port count number. Yang *et al.* [17] demonstrated a 4×4 switch fabric using four MZI switch elements. The footprint of the switch fabric was 0.8 mm × 0.8 mm. The demonstrated SNR (crosstalk) exceeded 15 dB. With integrated TO switches, the demonstrated switching time was ~10 μs.

Most notably, Lee *et al.* [18] demonstrated MZI-based 4×4 and 8×8 switch fabrics that were monolithically integrated with digital CMOS logic and device drivers using IBM's 90 nm silicon integrated nanophotonics technology. This is the first work demonstrating the feasibility of monolithically integrating CMOS logic and device drivers on the same chip as the switch fabric. They have delivered reconfiguration times below 5 ns using integrated EO switches with a power consumption of under 2 mW.

2. Switch Fabrics Using Microrings

Sherwood-Droz *et al.* [19] reported the first microring-based 4×4 silicon switch fabric in 2008. Their switch fabric comprised eight microring resonators in total, with four 1×2 switches each using a single microring coupled at a waveguide crossing and two 2×2 switches each using two microrings coupled at a waveguide crossing. The switch fabric occupied a small footprint of only 0.07 mm^2. The switch ER was below −20 dB, with a power consumption of ~6.5 mW/switch and a transmission bandwidth of ~38 GHz.

Yang *et al.* [20] also utilized microring resonators as the basic building blocks for their 4×4 switch fabric, comprising only four microrings. The demonstrated transmission data rate was 25 Gb/s/channel, with a crosstalk of −13.0 to −20.1 dB.

To address the shortcoming of the Lorentzian passband for a single microring, DasMahapatra *et al.* [22] demonstrated a 4×4 nonblocking switch fabric with each of the switch elements comprising five coupled microring resonators. The implementation of fifth-order microring resonators has reduced the crosstalk of a single switch element to below −27 dB. However, the use of five microrings as each switch element resulted in an enlarged footprint of 12 mm × 12 mm.

E. Active Resonance Wavelength Stabilization for Microrings

Although silicon-microring-based $N \times N$ switch fabrics can be promising in terms of switch power consumption and footprint, one major hurdle to overcome before practical applications is that the resonance wavelengths of each microring resonator in the switch fabric are sensitive to dynamic variations of the chip operational conditions, including the chip temperature and laser wavelengths. This results in misalignment between the resonance wavelength and the laser wavelength, which potentially leads to a significant compromise of the switch fabric's performance. To mitigate this problem, various methods including passive and active resonance wavelength stabilization methods have been developed.

Passive resonance wavelength stabilization methods, including (i) the use of claddings with a negative TO coefficient [105–108] and (ii) coupling the microresonator to an asymmetric MZI [109,110], have been studied by various research groups to stabilize the resonance wavelength upon temperature modulations. For (i), the claddings with a negative TO coefficient on silicon microring resonators counterbalance the silicon waveguide core's positive TO coefficient, resulting in thermal-insensitive microring resonators given a proper design. Specifically, polymers [105,106] and TiO_2 [107,108] are commonly used cladding materials with a negative TO coefficient. The resonance wavelength thermal dependence can be reduced to ~pm/°C. However, the method typically imposes a narrow waveguide width of below 300 nm in order to expose a sufficient fraction of the optical mode into the cladding layer. Thus, such a cladded athermal silicon waveguide cannot be readily integrated with other silicon photonic devices with a typical waveguide width of 400–500 nm. In addition, the athermal condition is highly dependent on the exact waveguide dimensions (width and height), making the approach not tolerant to fabrication imperfections.

For (ii), coupling the microresonator to one arm of an asymmetric MZI partially cancels the thermal-induced phase shift. However, as this method requires coupling a single microresonator to an asymmetric MZI, an extra footprint is required. When applying this passive method to N-by-N switch fabrics, we will significantly increase the footprint budget.

To avoid the shortcomings of the passive methods, various research groups, including our group, are currently seeking different active resonance wavelength stabilization methods to address this issue.

To date, four methods have been demonstrated to actively stabilize silicon microring resonators, including (i) a threshold-detection method for modulators by Zheng *et al.* [111], (ii) a dithering-signal detection method by Padmaraju and co-workers [112,113], (iii) a balanced homodyne detection method by Cox *et al.* [114], and (iv) a threshold-detection method and a related slope-detection method for switches and routers by Li and colleagues [115–118]. All these methods involved utilizing a photodetector as a monitor of the resonance wavelength alignment, an EO and/or TO tuner integrated with the microring for realignment, and a feedback-control circuit to control the tuners. For method (iii), however, given the homodyne detection imposed the use of a MZI for each microring, it may not be applicable for high-port-count $N \times N$ switch fabrics, and thus we do not review the work in detail here. Figure 9 shows the basic implementations of the other three active resonance wavelength stabilization schemes.

Zheng *et al.* [111] adopted a threshold-detection method to actively stabilize a microring-based modulator. They have flip-chip bonded the microring resonator with a CMOS chip including a 10 GHz driver, a bang-bang controller, and a digital-to-analog converter (DAC), as shown in Fig. 9(a). The bang-bang controller compared the measured photocurrent value from the photomonitor with a preset threshold and provided discrete signals at levels +1 or −1 to represent the alignment of the microring resonator. They have demonstrated a resonance-wavelength-locked 10 Gb/s modulator with a 4.5 nm locking range. However, the drawback of this threshold-detection method is that it is sensitive to variations in the input optical power.

In order to be tolerant to input optical power variations, Padmaraju *et al.* [112] used a dithering-signal method to monitor the resonance wavelength alignment of the microring, which was subjected to a small thermal modulation through an integrated TO tuner, as shown in Fig. 9(b). One can determine the degree of resonance alignment through mixing the modulated optical signal and the original driving dither signal. They reported microring resonance wavelength stabilization upon a 10 Hz sinusoidal signal with a 5 K temperature modulation. However, the dithering-signal method imposes an additional small modulation to the microring and needs complex electronics to facilitate dithering-signal generation and detection.

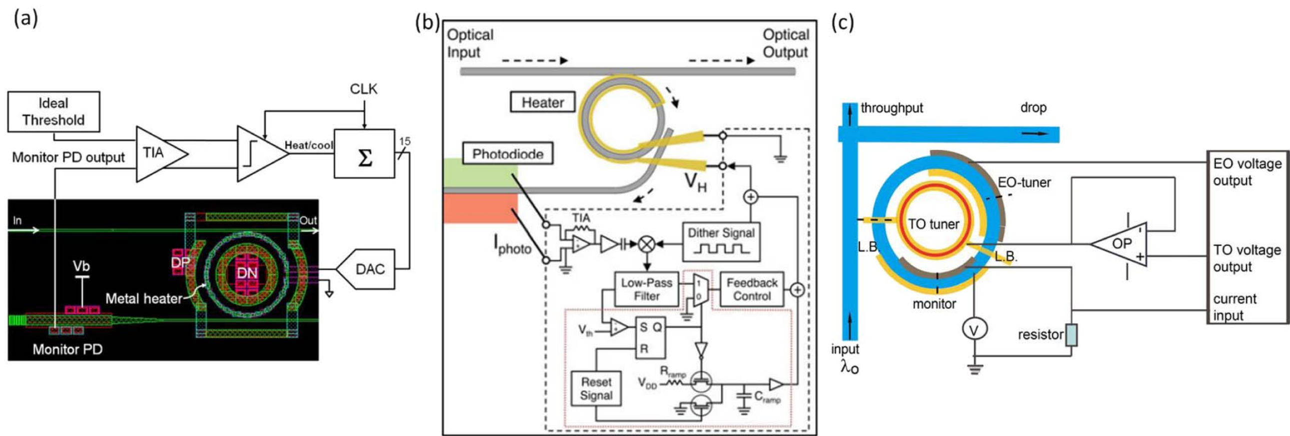

Fig. 9. Active resonance wavelength stabilization schemes for silicon microring resonators. (a) Threshold-detection method by Zheng *et al.* [111]. Reproduced with permission, © Optical Society of America 2014. (b) Dithering-signal method by Padmaraju *et al.* [112]. Reproduced with permission, © IEEE 2013. (c) Threshold-detection method by Li *et al.* [118]. L.B.: leakage block.

Notably, both methods reviewed above utilized an off-resonator photodetector as a monitor, which cannot be readily scaled for monitoring individual microrings in a large-scale-integrated photonic network or $N \times N$ switch fabric [14].

To address the issue of enabling large-scale integration, our research group (Li *et al.* [115,117]) have demonstrated a method utilizing an in-resonator photodetector as a monitor, which promises scaling of the technology to actively stabilize a large number of microrings in a photonic network or a switch fabric. The photodetector uses surface-state absorption (SSA) and defect-state absorption (DSA) in ion-implanted silicon microrings for sub-bandgap absorption in 1550 nm, and uses the microring cavity modes to enhance the photocurrent generation at resonances [115]. Hence, by comparing the measured in-resonator photocurrent value at the laser wavelength from the predefined threshold, we can detect the misalignment from a microring resonance.

Figure 9(c) illustrates the basic implementation of our threshold-detection method using an in-resonator SSA/DSA photodetector, along with an integrated EO tuner and an integrated TO tuner. The EO and TO tuners allow microring resonance wavelength stabilization upon both temperature rise and fall. A microprocessor functions as the control unit. We demonstrated actively stabilized resonance transmission at a high data rate of up to 30 Gb/s under on-chip temperature rise from 23°C to 32°C and temperature fall from 23°C to 18°C, with an applied tuning voltage of below 2.4 V. Nonetheless, our threshold-detection method is still sensitive to input optical power variations. To address this, we are currently investigating a slope-detection method using the same in-resonator photodetection and microprocessor control unit, which we believe can be insensitive to the input optical power variations [116,118].

Table 8 summarizes the state-of-the-art methods and performance of active resonance wavelength stabilization for silicon microrings. We notice that all the methods demonstrated have utilized complex control units or systems that are difficult to integrate with high-port-count microring switch fabrics. One of the next logical major steps forward regarding feedback-control systems will involve simplifying the microprocessor- or controller-based system with the use of transistors-based circuits. Another logical step forward regarding integration will be replacing the external or flip-chip-bonded control units with monolithically integrated CMOS logic circuits, as we will briefly outline in Section 6.E.

6. PERSPECTIVES AND GRAND CHALLENGES

Here we discuss our perspectives on future developments of silicon and hybrid silicon photonics for datacenter applications and highlight some grand challenges related to hybrid silicon lasers and silicon switch fabrics.

Table 7. Key Methods and Performance of State-of-the-Art High-Port-Count Silicon Switch Fabrics

References	Institution	Switch Elements	Topology	Crosstalk (dB)	Insertion Loss/Switch (dB)	Data Rate (Gb/s)	Reconfig. Time (μs)	Power Consump. (mW)[a]	Footprint (mm^2)	Self Connect.
Lu *et al.* [15]	SJTU, China	MZI	4 × 4 Beneš	< − 10	∼ − 3.3	NA	NA	4.5–8.1	3.5 × 1.4	Y
Chen *et al.* [16]	Alcatel-Lucent, USA	MZI	8 × 8 switch-and-select	∼ − 20	∼ − 0.33	NA	∼250	∼1.5	8 × 8	Y
Yang *et al.* [17]	CAS, China	MZI	4 × 4 with 4 MZIs	∼ − 15	∼ − 0.3	32	∼19	10–45	0.8 × 0.8	N
Lee *et al.* [18]	IBM, USA	MZI	4 × 4 8 × 8	< − 15	∼ − 3.7	16	<0.005	<2	0.165 (4 ports) 0.675 (8 ports)	Y
Droz *et al.* [19]	U Columbia, USA	Microring	4 × 4 with 8 rings	∼ − 20	< − 1.3	>38.5	NA	6.5	0.07	N
Yang *et al.* [20]	CAS, China	Microring	4 × 4 with 4 rings	< − 13	NA	25	∼10	NA	NA	N
DasMahapatra *et al.* [22]	TUE, Netherlands	Microring	4 × 4 cross bar	< − 27	∼ − 1.7	10	NA	NA	12 × 12	Y

[a]Including only the power consumption in switching routing states.

Table 8. Key Methods and Performance of Active Resonance Wavelength Stabilization Schemes for Silicon Microresonators

References	Institution	Device	Method	Control Unit	Monitor Integration	Temp. Range (K)	Data Rate (Gb/s)	Power Consump. (mW/K)
Zheng*et al.* [111]	Oracle, USA	Modulators	Threshold-detection	Bang-bangcontroller	Off-resonator	>50(4.5 nm)	10	0.24
Padmaraju *et al.* [112]	U Columbia, USA	Switches/filters	Dithering signals	PID controller	Off-resonator	5	10	NA
Li *et al.*[115]	HKUST, HK	Switches/filters	Threshold-detection	Microprocessor	In-resonator	14(18–32 °C)	30	~0.2 (EO) ~1.32 (TO)
Li *et al.*[118]	HKUST, HK	Switches/filters	Slope-detection	Microprocessor	In-resonator	7	NA	~0.2 (EO) ~1.32 (TO)

A. Energy Consumption

For on-chip hybrid silicon lasers, the most challenging issue is still the power consumption. None of the hybrid silicon lasers demonstrated to date meets the requirements listed in Section 4.A. The closest one is from a DM DFB laser bonded on a silicon substrate [83]. It consumed ~500 fJ/bit energy at 25.8 Gb/s with ~0.5 mW output power. Improving the direct modulation bandwidth is crucial to attaining low energy consumption for DM lasers. We can make meaningful improvements through increasing the confinement factor in the QW regions [83] or leverage the photon–photon resonance [84] through proper laser cavity design.

Other types of small-volume high-quality-factor (high-Q) laser cavities also promise more energy efficient hybrid silicon lasers. Takeda *et al.* [53] have reported a record-low threshold current of 31 μA on a photonic crystal cavity laser bonded on a silicon substrate. Such a type of small-volume high-Q hybrid silicon laser offers the possibility of ~10 fJ/bit power consumption, as previously demonstrated on the III–V substrate [119].

We also expect continuous efforts in improving on-chip high-speed photodetector sensitivity as well as transmission loss from the MUX/DeMUX and the fiber–waveguide coupling interfaces. Thus, we are optimistic that the energy-consumption requirements for on-chip lasers and transmitters can be relaxed in the future.

B. Thermal Management and Lasing Wavelength Control

Another important issue is the thermal control of on-chip lasers. To avoid the excessive cooling power for the lasers, uncooled and stable operation of the lasers up to ~70°C is desired. However, most of the demonstrated hybrid silicon lasers or laser arrays cannot work or suffer large performance degradation at this elevated temperature. This is partly due to the poor heat dissipation resulting from the wafer bonding. Effective thermal management needs to be further explored toward, preferably, uncooled operation.

The lasing wavelength control is also crucial, particularly when the on-chip lasers are working uncooled. Passive wavelength locking schemes following an athermal laser cavity design or active wavelength monitoring and locking schemes are needed, preferably with no or minimum extra power consumption. Alternatively, a frequency-comb laser as a master coherent multiwavelength laser source [Fig. 2(c)] are promising in terms of potentially enabling simple wavelength control. Mechanisms to equalize and maximize the output power from each wavelength channel are crucial to make multiwavelength transmitters practical for WDM optical interconnects.

C. New Materials and Integration

For the low threshold and high temperature operation requirements of on-chip lasers, III–V QDs as gain material seem to be a more promising solution than the widely adopted QWs as gain material for hybrid silicon lasers. A sub-kA/cm^2 threshold current density and a working temperature of up to 120°C have been reported on QD platforms [68]. High-quality and uniform QDs are required to obtain reliable and energy-efficient lasing.

Currently, hybrid-silicon-photonics-based integrated devices show a lower degree of integration compared to InP-based ones, so they are not cost effective. Further integration on 300 mm silicon wafers with a reduced single chip size are perhaps what is required to make the hybrid silicon approach more competitive. Epitaxial growth of III–V gain materials on a 300 mm silicon wafer could be one promising avenue toward low-cost photonic integration.

D. Number of Ports in a Switch Fabric

The number of port counts in a silicon switch fabric is, however, partially limited by the choice of switch fabric topologies and the switch elements, as we reviewed in Section 5, and partially limited by the available number of laser carrier wavelengths. The channel wavelength spacing and the wavelength span determine the number of laser carrier wavelengths. Following the ITU grid for DWDM applications, we can adopt 200 GHz channel spacing (~1.6 nm in 1550 nm) for 25 Gb/s/channel data transmission. If we suppose a laser wavelength span of 300 nm spanning the 1300–1600 nm communications band (where silicon is essentially transparent), the number of laser carrier wavelengths is ~187. Therefore, if each transceiver comprises four laser wavelengths, the number of port counts N the switch fabric needs to support is ~46 without any wavelength channel overlap.

For a microring-resonator-based switch with a Lorentzian-shape passband, which is not a "box-like" passband, a wide channel spacing of ~1.6 nm is necessary. However, if the passband of the microring can be shaped to a "box-like" passband, such as through a high-order coupled-microring-based switch element, the channel spacing could be narrowed to 0.8 nm following the 100 GHz ITU grid. In this case, the port count in a switch fabric can be increased to ~92, at the expense of an enlarged footprint and switch element complexity and

reliability. In principle, a larger port count is possible should we devise a different scheme in assigning laser carrier wavelengths to each of the transmitters or with the assistance of advanced data formats or routing algorithms.

E. Photonics-to-Electronics Convergence

Photonics-to-electronics (P-to-E) convergence is another key aspect that merits continuous concerted effort from industry and academia toward better optical interconnects in general, and especially toward the realization of high-port-count switch fabrics that require parallel active control for reconfiguration and stabilization. As reviewed in Section 5, the state of the art in controlling the silicon photonic interconnects still requires external or flip-chip-bonded control units, which are hardly scalable for high-port-count switch fabrics. A major opportunity for technology breakthroughs should leverage the compatibility of silicon photonics with CMOS electronics to converge the two monolithically on the same chip. The monolithic photonics–electronics integration is expected to enable major advantages, including active control functionalities, denser photonic and electronic device integration, lower energy consumption, higher bandwidth, and potentially lower manufacturing cost.

In 2012, IBM successfully monolithically integrated silicon modulators and Ge photodetectors with CMOS integrated circuit (IC)s using IBM's 90 nm technology node [120]. However, such early attempt in P-to-E convergence required stacks of layers and plenty of interlayer metal wires to allow the coexistence of transistors, Ge photodetectors, and silicon waveguides. If high-port-count silicon switch fabrics and optical interconnects in general are to be developed as we propose here, we will need a high density of electronic ICs serving as the laser and modulator drivers, the transimpedance amplifiers, and the switch control. Obviously, this still requires significant developments from both the photonic–electronic device design and process integration.

Another promising way to realize P-to-E convergence is to bond the separately fabricated electronic chip and photonic chip. In 2010, Oracle developed a hybrid flip-chip bonding method to bond a silicon photonic chip comprising silicon modulators and germanium waveguide photodetectors with an electronic chip comprising control circuits [121]. The main advantage of this method is that it allows the silicon photonic chip and the electronics to be separately fabricated in current mature fabrication technology platforms. However, the bonding introduces latency and parasitics, which limits the interconnect bandwidth. Researchers are currently developing various bonding methods to reduce the latency, including flip-chip bonding and through-silicon bias. It is still an open question which approaches P-to-E convergence will take, monolithic integration or bonding, for realizing high-port-count optical interconnections.

7. CONCLUSION

In this paper, we have reviewed the state of the art and our perspectives on silicon and hybrid silicon photonic devices for optical interconnect applications in datacenters. We outlined the key requirements for intra-datacenter optical interconnects. We put forth our vision of a WDM-based optical interconnect using hybrid silicon multiwavelength DM transmitters and high-port-count silicon switch fabrics. We gave a snapshot review of recent developments for the technologies that constitute the basis of our proposed concept. For hybrid silicon lasers and WDM transmitters, we have reviewed the state of the art and outlined the remaining challenges and issues toward low power consumption, direct modulation, and integration of multiwavelength laser arrays. For silicon switch fabrics, we evaluated different network topologies, including Beneš, cross bar, switch-and-select, and dilated Banyan, toward the realization of high-port-count switch fabrics, and we reviewed the state of the art. We discussed two common switch elements, namely, MZIs and microring resonators. We believe that the silicon microring, with a compact size and lower power consumption, is a promising candidate for realizing high-port-count switch fabrics. With this consideration, we also discussed the reliability of switch fabrics using microring resonators. We reviewed the state-of-the-art active resonance wavelength stabilization schemes for silicon microrings. Last, we proposed and discussed several grand challenges to be solved for intra-datacenter optical interconnects regarding energy consumption, thermal issues, laser wavelength control and material platforms of hybrid silicon lasers and transmitters, the number of ports a switch fabric can support, and, finally, the current trends and issues toward photonics-to-electronics convergence.

ACKNOWLEDGMENTS

This review paper was made possible partially by financial support from the National Science Foundation of China (NSFC) and the Research Grants Council (RGC) of the Hong Kong Special Administrative Region (HKSAR) under project N_HKUST606/10; the State Key Laboratory on Integrated Optoelectronics, China, Open Fund of the State Key Laboratory on Integrated Optoelectronics under project IOSKL2013KF04; the Innovation and Technology Fund (ITF) of the HKSAR under project ITS/023/14 and ITS/087/13; the Proof-of-Concept Fund (PCF) of The Hong Kong University of Science and Technology (HKUST) under project no. PCF007.12/13; and the General Research Fund (GRF) of the HKSAR under project no. 16208114. L. Zhang gratefully acknowledges postdoctoral fellowship support from the Hong Kong Scholars Program 2013. We gratefully acknowledge Nanoelectronics Fabrication Facility (NFF) of HKUST for fabricating the microspiral lasers and the actively stabilized silicon microring resonators reviewed here. We also gratefully acknowledge early contributions by Dr. Yue-De Yang and Prof. Yong-Zhen Huang on the microspiral lasers work.

REFERENCES

1. A. Ghiasi, "Large data centers interconnect bottlenecks," Opt. Express **23**, 2085–2090 (2015).
2. D. Nikolova, S. Rumley, D. Calhoun, Q. Li, R. Hendry, P. Samadi, and K. Bergman, "Scaling silicon photonic switch fabrics for data center interconnection networks," Opt. Express **23**, 1159–1175 (2015).
3. Finisar, http://www.finisar.com/products/active-cables.
4. Fujitsu, http://www.fujitsu.com/us/news/pr/fcai_20140304-01.html.
5. A. Alduino, L. Liao, R. Jones, M. Morse, B. Kim, W.-Z. Lo, J. Basak, B. Koch, H.-F. Liu, and H. Rong, "Demonstration of a high speed 4-channel integrated silicon photonics WDM link with hybrid silicon lasers," in *Integrated Photonics Research, Silicon and Nanophotonics* (Optical Society of America, 2010), paper PDIWI5.

6. G. A. Fish and D. K. Sparacin, "Enabling flexible datacenter interconnect networks with WDM silicon photonics," in *2014 IEEE Proceedings of the Custom Integrated Circuits Conference (CICC)*, San Jose, CA (IEEE, 2014).
7. R. Soref, "The past, present, and future of silicon photonics," IEEE J. Sel. Top. Quantum Electron. **12**, 1678–1687 (2006).
8. G. T. Reed and A. P. Knights, *Silicon Photonics: An Introduction* (Wiley, 2004).
9. Y. A. Vlasov, "Silicon CMOS-integrated nano-photonics for computer and data communications beyond 100G," IEEE Commun. Mag. **50**(2), s67–s72 (2012).
10. Y. Takahashi, T. Asano, D. Yamashita, and S. Noda, "Ultracompact 32-channel drop filter with 100 GHz spacing," Opt. Express **22**, 4692–4698 (2014).
11. D. Tan, A. Grieco, and Y. Fainman, "Towards 100 channel dense wavelength division multiplexing with 100 GHz spacing on silicon," Opt. Express **22**, 10408–10415 (2014).
12. G. T. Reed, D. J. Thomson, F. Y. Gardes, Y. Hu, J.-M. Fedeli, and G. Z. Mashanovich, "High-speed carrier-depletion silicon Mach-Zehnder optical modulators with lateral PN junctions," Front. Phys. **2**, 77 (2014).
13. D. Marris-Morini, L. Virot, C. Baudot, J.-M. Fédéli, G. Rasigade, D. Perez-Galacho, J.-M. Hartmann, S. Olivier, P. Brindel, and P. Crozat, "A 40 Gbit/s optical link on a 300-mm silicon platform," Opt. Express **22**, 6674–6679 (2014).
14. A. W. Poon, X. Luo, F. Xu, and H. Chen, "Cascaded microresonator-based matrix switch for silicon on-chip optical interconnection," Proc. IEEE **97**, 1216–1238 (2009).
15. L. Lu, L. Zhou, Z. Li, X. Li, and J. Chen, "Broadband 4×4 nonblocking silicon electro-optic switches based on Mach-Zehnder interferometers," IEEE Photon. J. **7**, 7800108 (2015).
16. L. Chen and Y.-K. Chen, "Compact, low-loss and low-power 8×8 broadband silicon optical switch," Opt. Express **20**, 18977–18985 (2012).
17. L. Yang, Y. Xia, F. Zhang, Q. Chen, J. Ding, P. Zhou, and L. Zhang, "Reconfigurable non-blocking 4-port silicon thermo-optic optical router based on Mach-Zehnder optical switches," Opt. Lett. **40**, 1402–1405 (2015).
18. B. G. Lee, A. V. Rylyakov, W. M. Green, S. Assefa, C. W. Baks, R. Rimolo-Donadio, D. M. Kuchta, M. H. Khater, T. Barwicz, and C. Reinholm, "Monolithic silicon integration of scaled photonic switch fabrics, CMOS logic, and device driver circuits," J. Lightwave Technol. **32**, 743–751 (2014).
19. N. Sherwood-Droz, H. Wang, L. Chen, B. G. Lee, A. Biberman, K. Bergman, and M. Lipson, "Optical 4×4 hitless silicon router for optical networks-on-chip (NoC)," Opt. Express **16**, 15915–15922 (2008).
20. L. Yang, H. Jia, Y. Zhao, and Q. Chen, "Reconfigurable nonblocking four-port optical router based on microring resonators," Opt. Lett. **40**, 1129–1132 (2015).
21. A. Biberman, B. G. Lee, N. Sherwood-Droz, M. Lipson, and K. Bergman, "Broadband operation of nanophotonic router for silicon photonic networks-on-chip," IEEE Photon. Technol. Lett. **22**, 926–928 (2010).
22. P. DasMahapatra, A. Rohit, R. Stabile, and K. A. Williams, "Broadband 4×4 switch matrix using fifth-order resonators," in *Optical Fiber Communication Conference/National Fiber Optic Engineers Conference 2013*, OSA Technical Digest (online) (Optical Society of America, 2013), paper OW3H.2.
23. L. Vivien, A. Polzer, D. Marris-Morini, J. Osmond, J. M. Hartmann, P. Crozat, E. Cassan, C. Kopp, H. Zimmermann, and J. M. Fédéli, "Zero-bias 40 Gbit/s germanium waveguide photodetector on silicon," Opt. Express **20**, 1096–1101 (2012).
24. N.-N. Feng, D. Feng, S. Liao, X. Wang, P. Dong, H. Liang, C.-C. Kung, W. Qian, J. Fong, and R. Shafiiha, "30 GHz Ge electroabsorption modulator integrated with 3 μm silicon-on-insulator waveguide," Opt. Express **19**, 7062–7067 (2011).
25. F. Bonaccorso, Z. Sun, T. Hasan, and A. Ferrari, "Graphene photonics and optoelectronics," Nat. Photonics **4**, 611–622 (2010).
26. R. E. Camacho-Aguilera, Y. Cai, N. Patel, J. T. Bessette, M. Romagnoli, L. C. Kimerling, and J. Michel, "An electrically pumped germanium laser," Opt. Express **20**, 11316–11320 (2012).
27. S. Wirths, R. Geiger, N. von den Driesch, G. Mussler, T. Stoica, S. Mantl, Z. Ikonic, M. Luysberg, S. Chiussi, J. M. Hartmann, H. Sigg, J. Faist, D. Buca, and D. Grützmacher, "Lasing in direct-bandgap GeSn alloy grown on Si," Nat. Photonics **9**, 88–92 (2015).
28. K. Yamada, T. Tsuchizawa, H. Nishi, R. Kou, T. Hiraki, K. Takeda, H. Fukuda, Y. Ishikawa, K. Wada, and T. Yamamoto, "High-performance silicon photonics technology for telecommunications applications," Sci. Technol. Adv. Mater. **15**, 024603 (2014).
29. D. Feng, W. Qian, H. Liang, B. Luff, and M. Asghari, "High-speed receiver technology on the SOI platform," IEEE J. Sel. Top. Quantum Electron. **19**, 3800108 (2013).
30. P. Dong, Y.-K. Chen, G.-H. Duan, and D. T. Neilson, "Silicon photonic devices and integrated circuits," Nanophotonics **3**, 215–228 (2014).
31. A. Alduino, "Demonstration of a high speed 4-channel integrated silicon photonics WDM link with hybrid silicon lasers," in *Hot Chips: A Symposium on High Performance Chips*, Stanford, CA (2010).
32. "Cisco Visual Networking Index: Forecast and Methodology, 2013–2018," http://www.cisco.com/c/en/us/solutions/collateral/service-provider/ip-ngn-ip-next-generation-network/white_paper_c11-481360.html.
33. N. Ophir, C. Mineo, D. Mountain, and K. Bergman, "Silicon photonic microring links for high-bandwidth-density, low-power chip I/O," IEEE Micro **33**, 54–67 (2013).
34. "IEEE standard for information technology-telecommunications and information exchange between systems-local and metropolitan area networks-specific requirements part 3: carrier sense multiple access with collision detection (CSMA/CD) access method and physical layer specifications amendment 4: media access control parameters, physical layers and management parameters for 40 Gb/s and 100 Gb/s operation," IEEE Standard 802.3ba-2010 (amendment to IEEE Standard 802.3-2008).
35. "100 G CWDM4 MSA Technical Specifications" (2014), http://www.cwdm4-msa.org/files/CWDM4_MSA_Technical_Spec_1p0.pdf.
36. G. Li, A. V. Krishnamoorthy, I. Shubin, J. Yao, Y. Luo, H. Thacker, X. Zheng, K. Raj, and J. E. Cunningham, "Ring resonator modulators in silicon for interchip photonic links," IEEE J. Sel. Top. Quantum Electron. **19**, 95–113 (2013).
37. L. Pavesi, L. Dal Negro, C. Mazzoleni, G. Franzo, and F. Priolo, "Optical gain in silicon nanocrystals," Nature **408**, 440–444 (2000).
38. S. G. Cloutier, P. A. Kossyrev, and J. Xu, "Optical gain and stimulated emission in periodic nanopatterned crystalline silicon," Nat. Mater. **4**, 887–891 (2005).
39. A. W. Fang, M. N. Sysak, B. R. Koch, R. Jones, E. Lively, Y. H. Kuo, D. Liang, O. Raday, and J. E. Bowers, "Single-wavelength silicon evanescent lasers," IEEE J. Sel. Top. Quantum Electron. **15**, 535–544 (2009).
40. C. Zhang, S. Srinivasan, Y. B. Tang, M. J. R. Heck, M. L. Davenport, and J. E. Bowers, "Low threshold and high speed short cavity distributed feedback hybrid silicon lasers," Opt. Express **22**, 10202–10209 (2014).
41. S. Matsuo, T. Fujii, K. Hasebe, K. Takeda, T. Sato, and T. Kakitsuka, "Directly modulated buried heterostructure DFB laser on SiO_2/Si substrate fabricated by regrowth of InP using bonded active layer," Opt. Express **22**, 12139–12147 (2014).
42. D. Liang, G. Kurczveil, C. H. Chen, M. Fiorentino, Z. Peng, and R. G. Beausoleil, "Silicon photonic integrated devices for optical interconnects" (2013), http://www.hpl.hp.com/techreports/2013/HPL-2013-56.pdf.
43. D. Liang, S. Srinivasan, D. A. Fattal, M. Fiorentino, Z. H. Huang, D. T. Spencer, J. E. Bowers, and R. G. Beausoleil, "Teardrop reflector-assisted unidirectional hybrid silicon microring lasers," IEEE Photon. Technol. Lett. **24**, 1988–1990 (2012).
44. B. R. Koch, E. J. Norberg, B. Kim, J. Hutchinson, J.-H. Shin, G. Fish, and A. Fang, "Integrated silicon photonic laser sources for telecom and datacom," in *National Fiber Optic Engineers Conference* (Optical Society of America, 2013), paper PDP5C. 8.
45. G. Kurczveil, M. J. Heck, J. D. Peters, J. M. Garcia, D. Spencer, and J. E. Bowers, "An integrated hybrid silicon multiwavelength AWG laser," IEEE J. Sel. Top. Quantum Electron. **17**, 1521–1527 (2011).
46. G.-H. Duan, C. Jany, A. Le Liepvre, A. Accard, M. Lamponi, D. Make, P. Kaspar, G. Levaufre, N. Girard, and F. Lelarge, "Hybrid

III-V on silicon lasers for photonic integrated circuits on silicon," IEEE J. Sel. Top. Quantum Electron. **20**, 158–170 (2014).
47. S. Keyvaninia, G. Roelkens, D. Van Thourhout, C. Jany, M. Lamponi, A. Le Liepvre, F. Lelarge, D. Make, G.-H. Duan, D. Bordel, and J.-M. Fedeli, "Demonstration of a heterogeneously integrated III-V/SOI single wavelength tunable laser," Opt. Express **21**, 3784–3792 (2013).
48. P. Dong, T.-C. Hu, T.-Y. Liow, Y.-K. Chen, C. Xie, X. Luo, G.-Q. Lo, R. Kopf, and A. Tate, "Novel integration technique for silicon/III-V hybrid laser," Opt. Express **22**, 26854–26861 (2014).
49. D. Liang, S. Srinivasan, M. Fiorentino, G. Kurczveil, J. E. Bowers, and R. G. Beausoleil, "A metal thermal shunt design for hybrid silicon microring laser," in *IEEE Optical Interconnects Conference* (IEEE, 2012), pp. 20–23.
50. C. Zhang, D. Liang, G. Kurczveil, J. Bowers, and R. Beausoleil, "High Temperature Hybrid Silicon Micro-ring Lasers with Thermal Shunts," in *Conference on Lasers and Electro-Optics*, *CLEO: 2015*, OSA Technical Digest (online) (Optical Society of America, 2015), paper SW3F.5.
51. M. N. Sysak, D. Liang, R. Jones, G. Kurczveil, M. Piels, M. Fiorentino, R. G. Beausoleil, and J. E. Bowers, "Hybrid silicon laser technology: A thermal perspective," IEEE J. Sel. Top. Quantum Electron. **17**, 1490–1498 (2011).
52. H.-H. Chang, A. W. Fang, M. N. Sysak, H. Park, R. Jones, O. Cohen, O. Raday, M. J. Paniccia, and J. E. Bowers, "1310 nm silicon evanescent laser," Opt. Express **15**, 11466–11471 (2007).
53. K. Takeda, T. Sato, T. Fujii, E. Kuramochi, M. Notomi, K. Hasebe, T. Kakitsuka, and S. Matsuo, "Heterogeneously integrated photonic-crystal lasers on silicon for on/off chip optical interconnects," Opt. Express **23**, 702–708 (2015).
54. J. Van Campenhout, P. Rojo-Romeo, P. Regreny, C. Seassal, D. Van Thourhout, S. Verstuyft, L. Di Cioccio, J. M. Fedeli, C. Lagahe, and R. Baets, "Electrically pumped InP-based microdisk lasers integrated with a nanophotonic silicon-on-insulator waveguide circuit," Opt. Express **15**, 6744–6749 (2007).
55. J. Van Campenhout, L. Liu, P. R. Romeo, D. Van Thourhout, C. Seassal, P. Regreny, L. Di Cioccio, J. M. Fedeli, and R. Baets, "A compact SOI-integrated multiwavelength laser source based on cascaded InP microdisks," IEEE Photon. Technol. Lett. **20**, 1345–1347 (2008).
56. Y. Huang, S. Sui, M. Tang, Y. Yang, J. Xiao, and Y. Du, "Sixteen-wavelength hybrid AlGaInAs/Si microdisk laser array," IEEE J. Sel. Top. Quantum Electron. **51**, 2600108 (2015).
57. S. Keyvaninia, S. Verstuyft, S. Pathak, F. Lelarge, G. H. Duan, D. Bordel, J. M. Fedeli, T. De Vries, B. Smalbrugge, E. J. Geluk, J. Bolk, M. Smit, G. Roelkens, and D. Van Thourhout, "III-V-on-silicon multi-frequency lasers," Opt. Express **21**, 13675–13683 (2013).
58. P. Mechet, S. Verstuyft, T. de Vries, T. Spuesens, P. Regreny, D. Van Thourhout, G. Roelkens, and G. Morthier, "Unidirectional III-V microdisk lasers heterogeneously integrated on SOI," Opt. Express **21**, 19339–19352 (2013).
59. F. Peng, Z. Yejin, W. Yufei, L. Lei, Z. Siriguleng, W. Hailing, and Z. Wanhua, "A novel hybrid III-V/silicon deformed micro-disk single-mode laser," J. Semicond. **36**, 055008 (2015).
60. Y. Zhang, Y.-D. Yang, Y.-Z. Huang, and A. W. Poon, "Directional-emission III-V-on-silicon microspiral and double-notch microdisk lasers for optical interconnects," in *Conference on Lasers and Electro-Optics*, *CLEO: Applications and Technology* (Optical Society of America, 2014), paper JTu4A.118.
61. A. W. Poon, Y. Zhang, and L. Zhang, "Hybrid silicon unidirectional-emission microspiral disk lasers for optical interconnect applications," Proc. SPIE **9343**, 934312 (2015).
62. G. Roelkens, D. Van Thourhout, and R. Baets, "Continuous-wave lasing from DVS-BCB heterogeneously integrated laser diodes," in *Integrated Photonics and Nanophotonics Research and Applications* (Optical Society of America, 2007), paper ITuG4.
63. P. Mechet, F. Raineri, A. Bazin, Y. Halioua, T. Spuesens, T. J. Karle, P. Regreny, P. Monnier, D. Van Thourhout, I. Sagnes, R. Raj, G. Roelkens, and G. Morthier, "Uniformity of the lasing wavelength of heterogeneously integrated InP microdisk lasers on SOI," Opt. Express **21**, 10622–10631 (2013).
64. L. Liu, G. Roelkens, J. Van Campenhout, J. Brouckaert, D. Van Thourhout, and R. Baets, "III-V/silicon-on-insulator nanophotonic cavities for optical network-on-chip," J. Nanosci. Nanotechnol. **10**, 1461–1472 (2010).
65. L. Tao, L. Yuan, Y. Li, H. Yu, B. Wang, Q. Kan, W. Chen, J. Pan, G. Ran, and W. Wang, "4-λ InGaAsP-Si distributed feedback evanescent lasers with varying silicon waveguide width," Opt. Express **22**, 5448–5454 (2014).
66. J. Ferrara, W. Yang, L. Zhu, P. Qiao, and C. J. Chang-Hasnain, "Heterogeneously integrated long-wavelength VCSEL using silicon high contrast grating on an SOI substrate," Opt. Express **23**, 2512–2523 (2015).
67. E. Marchena, T. Creazzo, S. B. Krasulick, P. Yu, D. Van Orden, J. Y. Spann, C. C. Blivin, J. M. Dallesasse, P. Varangis, R. J. Stone, and A. Mizrahi, "Integrated tunable CMOS laser for Si photonics," in *Optical Fiber Communication Conference/National Fiber Optic Engineers Conference 2013*, OSA Technical Digest (online) (Optical Society of America, 2013), paper PDP5 C.7.
68. A. Y. Liu, C. Zhang, J. Norman, A. Snyder, D. Lubyshev, J. M. Fastenau, A. W. Liu, A. C. Gossard, and J. E. Bowers, "High performance continuous wave 1.3 μm quantum dot lasers on silicon," Appl. Phys. Lett. **104**, 041104 (2014).
69. D. Liang, G. Roelkens, R. Baets, and J. E. Bowers, "Hybrid integrated platforms for silicon photonics," Materials **3**, 1782–1802 (2010).
70. S. Keyvaninia, M. Muneeb, S. Stanković, P. Van Veldhoven, D. Van Thourhout, and G. Roelkens, "Ultra-thin DVS-BCB adhesive bonding of III-V wafers, dies and multiple dies to a patterned silicon-on-insulator substrate," Opt. Mater. Express **3**, 35–46 (2013).
71. Dow Chemical, http://www.dow.com/cyclotene/solution/thermprop.htm.
72. Y. Zhang, S. Y. Yang, H. Guan, A. E. J. Lim, G. Q. Lo, P. Magill, T. Baehr-Jones, and M. Hochberg, "Sagnac loop mirror and micro-ring based laser cavity for silicon-on-insulator," Opt. Express **22**, 17872–17879 (2014).
73. J. H. Lee, I. Shubin, J. Yao, J. Bickford, Y. Luo, S. Y. Lin, S. S. Djordjevic, H. D. Thacker, J. E. Cunningham, K. Raj, X. Zheng, and A. V. Krishnamoorthy, "High power and widely tunable Si hybrid external-cavity laser for power efficient Si photonics WDM links," Opt. Express **22**, 7678–7685 (2014).
74. D. Liang, M. Fiorentino, S. T. Todd, G. Kurczveil, R. G. Beausoleil, and J. E. Bowers, "Fabrication of silicon-on-diamond substrate and low-loss optical waveguides," IEEE Photon. Technol. Lett. **23**, 657–659 (2011).
75. J. E. Bowers, J. T. Bovington, A. Y. Liu, A. C. Gossard, G. Li, T. Creazzo, E. Marchena, P. K. Yu, S. Krasulick, and L. Schares, "A path to 300 mm hybrid silicon photonic integrated circuits," in *Optical Fiber Communication Conference*, San Francisco, CA (IEEE, 2014).
76. S. Menezo, H. Duprez, A. Descos, D. Bordel, L. Sanchez, P. Brianceau, L. Fulbert, V. Carron, and B. Ben Bakir, "Advances on III-V on silicon DBR and DFB lasers for WDM optical interconnects and associated heterogeneous integration 200 mm-wafer-scale technology," in *2014 IEEE Compound Semiconductor Integrated Circuit Symposium (CSICs)*, La Jolla, CA (IEEE, 2014).
77. G. D. Chern, H. E. Tureci, A. D. Stone, R. K. Chang, M. Kneissl, and N. M. Johnson, "Unidirectional lasing from InGaN multiple-quantum-well spiral-shaped micropillars," Appl. Phys. Lett. **83**, 1710–1712 (2003).
78. M. Kneissl, M. Teepe, N. Miyashita, N. M. Johnson, G. D. Chern, and R. K. Chang, "Current-injection spiral-shaped microcavity disk laser diodes with unidirectional emission," Appl. Phys. Lett. **84**, 2485–2487 (2004).
79. L. Ge, O. Malik, and H. E. Türeci, "Enhancement of laser power-efficiency by control of spatial hole burning interactions," Nat. Photonics **8**, 871–875 (2014).
80. Y. D. Yang, Y. Zhang, Y. Z. Huang, and A. W. Poon, "Direct-modulated waveguide-coupled microspiral disk lasers with spatially selective injection for on-chip optical interconnects," Opt. Express **22**, 824–838 (2014).
81. D. A. B. Miller, "Energy consumption in optical modulators for interconnects," Opt. Express **20**, A293–A308 (2012).
82. W. Kobayashi, T. Ito, T. Yamanaka, T. Fujisawa, Y. Shibata, T. Kurosaki, M. Kohtoku, T. Tadokoro, and H. Sanjoh, "50-Gb/s direct modulation of 1.3-μm InGaAlAs-based DFB laser with

ridge waveguide structure," IEEE J. Sel. Top. Quantum Electron. **19**, 1500908 (2013).

83. S. Matsuo, T. Fujii, K. Hasebe, K. Takeda, T. Sato, and T. Kakitsuka, "40-Gbit/s direct modulation of membrane buried heterostructure DFB laser on SiO_2/Si substrate," in *2014 International Semiconductor Laser Conference (ISLC)* (IEEE, 2014), pp. 30–31.
84. G. de Valicourt, Y. Pointurier, J.-C. Antona, and G. Duan, "A 20 Gbit/s directly modulated hybrid III-V/Si laser tunable over 12 wavelengths for short-reach access network," in *2014 European Conference on Optical Communication (ECOC)* (IEEE, 2014).
85. J. H. Marsh, "Quantum well intermixing," Semicond. Sci. Technol. **8**, 1136–1155 (1993).
86. S. Srinivasan, A. W. Fang, D. Liang, J. Peters, B. Kaye, and J. E. Bowers, "Design of phase-shifted hybrid silicon distributed feedback lasers," Opt. Express **19**, 9255–9261 (2011).
87. B. R. Koch, A. W. Fang, E. Lively, R. Jones, O. Cohen, D. J. Blumenthal, and J. E. Bowers, "Mode locked and distributed feedback silicon evanescent lasers," Laser Photon. Rev. **3**, 355–369 (2009).
88. S. Srinivasan, A. Arrighi, M. J. Heck, J. Hutchinson, E. Norberg, G. Fish, and J. E. Bowers, "Harmonically mode-locked hybrid silicon laser with intra-cavity filter to suppress supermode noise," IEEE J. Sel. Top. Quantum Electron. **20**, 8–15 (2014).
89. M. A. Foster, J. S. Levy, O. Kuzucu, K. Saha, M. Lipson, and A. L. Gaeta, "Silicon-based monolithic optical frequency comb source," Opt. Express **19**, 14233–14239 (2011).
90. P. Dumais, J. Jiang, H. Mehrvar, D. Celo, D. Goodwill, and E. Bernier, "Performance optimization for switch matrices based on carrier-injection-driven Mach-Zehnder switch cells," in *2014 IEEE 11th International Conference on Group IV Photonics (GFP)* (IEEE, 2014), pp. 96–97.
91. B. G. Lee, N. Dupuis, P. Pepeljugoski, L. Schares, R. Budd, J. R. Bickford, and C. L. Schow, "Silicon photonic switch fabrics in computer communications systems," J. Lightwave Technol. **33**, 768–777 (2015).
92. H. Mehrvar, "Hybrid photonic ethernet switch for datacenters," in *Optical Fiber Communication Conference* (Optical Society of America, 2014), paper M3E.6.
93. L. Zhou, L. Lu, Z. Li, and J. Chen, "Broadband 4 × 4 non-blocking optical switch fabric based on Mach-Zehnder interferometers," in *2014 13th International Conference on Optical Communications and Networks (ICOCN)* (IEEE, 2014).
94. P. Dong, Y.-K. Chen, T. Gu, L. L. Buhl, D. T. Neilson, and J. H. Sinsky, "Reconfigurable 100 Gb/s silicon photonic network-on-chip," J. Opt. Commun. Netw. **7**, A37–A43 (2015).
95. L. Chen, E. Hall, L. Theogarajan, and J. Bowers, "Photonic switching for data center applications," IEEE Photon. J. **3**, 834–844 (2011).
96. S. S. Haykin, *Communication Systems* (Wiley, 2001).
97. IME, https://www.a-star.edu.sg/ime/.
98. IMEC, http://www2.imec.be/be_en/home.html.
99. Y. Shen, I. B. Divliansky, D. N. Basov, and S. Mookherjea, "Electric-field-driven nano-oxidation trimming of silicon microrings and interferometers," Opt. Lett. **36**, 2668–2670 (2011).
100. A. H. Atabaki, A. A. Eftekhar, M. Askari, and A. Adibi, "Accurate post-fabrication trimming of ultra-compact resonators on silicon," Opt. Express **21**, 14139–14145 (2013).
101. D. Bachman, Z. Chen, R. Fedosejevs, Y. Y. Tsui, and V. Van, "Permanent fine tuning of silicon microring devices by femtosecond laser surface amorphization and ablation," Opt. Express **21**, 11048–11056 (2013).
102. Q. Xu, D. Fattal, and R. G. Beausoleil, "Silicon microring resonators with 1.5-μm radius," Opt. Express **16**, 4309–4315 (2008).
103. P. Dong, S. Liao, H. Liang, R. Shafiiha, D. Feng, G. Li, X. Zheng, A. V. Krishnamoorthy, and M. Asghari, "Submilliwatt, ultrafast and broadband electro-optic silicon switches," Opt. Express **18**, 25225–25231 (2010).
104. H. Zhou, Y. Zhao, W. Wang, J. Yang, M. Wang, and X. Jiang, "Performance influence of carrier absorption to the Mach-Zehnder-interference based silicon optical switches," Opt. Express **17**, 7043–7051 (2009).
105. J. Teng, P. Dumon, W. Bogaerts, H. Zhang, X. Jian, X. Han, M. Zhao, G. Morthier, and R. Baets, "Athermal silicon-on-insulator ring resonators by overlaying a polymer cladding on narrowed waveguides," Opt. Express **17**, 14627–14633 (2009).
106. P. Alipour, E. S. Hosseini, A. A. Eftekhar, B. Momeni, and A. Adibi, "Athermal performance in high-Q polymer-clad silicon microdisk resonators," Opt. Lett. **35**, 3462–3464 (2010).
107. S. S. Djordjevic, K. Shang, B. Guan, S. T. S. Cheung, L. Liao, J. Basak, H.-F. Liu, and S. J. B. Yoo, "CMOS-compatible, athermal silicon ring modulators clad with titanium dioxide," Opt. Express **21**, 13958–13968 (2013).
108. B. Guha, J. Cardenas, and M. Lipson, "Athermal silicon microring resonators with titanium oxide cladding," Opt. Express **21**, 26557–26563 (2013).
109. B. Guha, K. Preston, and M. Lipson, "Athermal silicon microring electro-optic modulator," Opt. Lett. **37**, 2253–2255 (2012).
110. L. Lu, L. Zhou, X. Sun, J. Xie, Z. Zou, H. Zhu, X. Li, and J. Chen, "CMOS-compatible temperature-independent tunable silicon optical lattice filters," Opt. Express **21**, 9447–9456 (2013).
111. X. Zheng, E. Chang, P. Amberg, I. Shubin, J. Lexau, F. Liu, H. Thacker, S. S. Djordjevic, S. Lin, Y. Luo, J. Yao, J.-H. Lee, K. Raj, R. Ho, J. E. Cunningham, and A. V. Krishnamoorthy, "A high-speed, tunable silicon photonic ring modulator integrated with ultra-efficient active wavelength control," Opt. Express **22**, 12628–12633 (2014).
112. K. Padmaraju, D. F. Logan, T. Shiraishi, J. J. Ackert, A. P. Knights, and K. Bergman, "Wavelength locking and thermally stabilizing microring resonators using dithering signals," J. Lightwave Technol. **32**, 505–512 (2014).
113. X. Zhu, K. Padmaraju, L.-W. Luo, S. Yang, M. Glick, R. Dutt, M. Lipson, and K. Bergman, "Fast wavelength locking of a microring resonator," IEEE Photon. Technol. Lett. **26**, 2365–2368 (2014).
114. J. A. Cox, A. L. Lentine, D. C. Trotter, and A. L. Starbuck, "Control of integrated micro-resonator wavelength via balanced homodyne locking," Opt. Express **22**, 11279–11289 (2014).
115. Y. Li and A. W. Poon, "Active resonance wavelength stabilization for silicon microring resonators with an in-resonator defect-state-absorption-based photodetector," Opt. Express **23**, 360–372 (2015).
116. Y. Zhang, Y. Li, S. Feng, and A. Poon, "Towards adaptively tuned silicon microring resonators for optical networks-on-chip applications," IEEE J. Sel. Top. Quantum Electron. **20**, 136–149 (2014).
117. Y. Li, S. Feng, Y. Zhang, and A. W. Poon, "In-microresonator linear-absorption-based real-time photocurrent-monitoring and tuning with closed-loop control for silicon microresonators," U.S. patent application 14/057,679 (filed October 18, 2013).
118. Y. Li and A. W. Poon, "Active resonance wavelength stabilization for silicon microring resonators using slope-detection with an inresonator defect-state-absorption-based photodetector," in *Conference on Lasers and Electro-Optics* (Optical Society of America, 2015), paper SM2I.2
119. S. Matsuo, T. Sato, K. Takeda, A. Shinya, K. Nozaki, H. Taniyama, M. Notomi, K. Hasebe, and T. Kakitsuka, "Ultralow operating energy electrically driven photonic crystal lasers," IEEE J. Sel. Top. Quantum Electron. **19**, 4900311 (2013).
120. S. Assefa, S. Shank, W. Green, M. Khater, E. Kiewra, C. Reinholm, S. Kamlapurkar, A. Rylyakov, C. Schow, and F. Horst, "A 90 nm CMOS integrated nano-photonics technology for 25 Gbps WDM optical communications applications," in *IEEE International Electron Devices Meeting (IEDM)*, San Francisco, CA (IEEE, 2012).
121. H. D. Thacker, Y. Luo, J. Shi, I. Shubin, J. Lexau, X. Zheng, G. Li, J. Yao, J. Costa, and T. Pinguet, "Flip-chip integrated silicon photonic bridge chips for sub-picojoule per bit optical links," in *2010 Proceedings 60th Electronic Components and Technology Conference (ECTC)* (IEEE, 2010), pp. 240–246.